Title: Hippocampal spreading depolarization drives post-ictal ambulation

Authors: Bence Mitlasóczki[1,2], Adrián Gutiérrez Gómez[1], Midia Kamali[1,2], Natalia Babushkina[3,4], Mayan Baues[1,2], Laura Kück[1,2], André Nathan Haubrich[2], Theodoros Tamiolakis[1,2], Annika Breuer[1], Simon Granak[1], Merlin Schwering-Sohnrey[1,2], Ingo Gerhauser[5], Wolfgang Baumgärtner[5], Laura Ewell[6], Thoralf Opitz[2], Julika Pitsch[1], Simon Musall[2,3,4], Rainer Surges[1], Florian Mormann[1], Heinz Beck[2,7], Michael Wenzel[1,2*]

Affiliations:

1 University Hospital Bonn, Dept. of Epileptology, Bonn, Germany
2 University of Bonn, Medical Faculty, Institute of Experimental Epileptology and Cognition Research, Bonn, Germany
3 Institute of Biological Information Processing (IBI-3) – Bioelectronics Forschungszentrum, Jülich, Germany
4 Institute of Biology II, RWTH Aachen University, Aachen, Germany
5 Department of Pathology, University of Veterinary Medicine Hannover, Hannover, Germany
6 Department of Anatomy and Neurobiology, University of California, Irvine, USA
7 Deutsches Zentrum für Neurodegenerative Erkrankungen e.V., Bonn, Germany

***Correspondence to:**
Michael Wenzel
University Hospital Bonn, Dept. of Epileptology, Venusberg-Campus 1, 53127 Bonn, Germany
Email: michael.wenzel@ukbonn.de
Phone: +49 228 287 16954

Number of main figures: 5
Number of suppl. figures/tables: 11/3

Author approvals: All authors have seen and approved the manuscript, and the manuscript has not been accepted or published elsewhere.

Conflict of Interest: The authors declare no competing interests.

Abstract

Post-seizure (*post-ictal*) symptoms are regularly encountered in epilepsy, and can be life-threatening, yet their neurobiological underpinnings remain understudied. Using two-photon or widefield imaging, field potential and unit recordings, optogenetics, and basic behavioral assessment under healthy conditions or viral encephalitis, we studied seizures and post-ictal symptoms in mice. In addition, we analyzed Behnke-Fried depth-electrode recordings in an initial cohort of 4 patients with chronic epilepsy. In mice, we show a massive propensity of the hippocampus for seizure-associated spreading depolarization (sSD). Via optogenetic stimulation, we provide evidence that isolated hippocampal SD drives *post-ictal ambulation* (PIA), whereas optogenetic seizure-like episodes do not. Further, PIA occurred in the absence of SD progression to the neocortex. In support of our experiments in mice, we also found an increased vulnerability of the human temporomesial system (hippocampus, amygdala) for putative sSD at Sz termination, and differential recovery times of affected vs. non-affected brain regions. This work uncovers sSD as a previously underrecognized key pathoclinical entity underlying distinct postictal symptoms in epilepsy. Our results carry ramifications for epilepsy research and neurology, and challenge current EEG-standards.

Main Text:

Introduction

The post-ictal period often manifests with confusion, aphasia, amnesia, or unaware ambulation (*post-ictal wandering*), which is most commonly observed in temporal lobe epilepsy (TLE, ~25-45%)(*1*–*4*), and associated with a risk of potentially life-threatening injuries(*1*, *5*). Despite the far-reaching clinical and socio-economic impact (*1*, *2*), except for particular entities such as sudden unexpected death in epilepsy (SUDEP)(*6*, *7*), the neurobiological underpinnings of the post-ictal state remain unclear, and most related research on this topic has focused on consequence rather than initial cause(*8*, *9*). One reason for the continued scarcity of neurobiological insight may be that the *ictus* itself has continually formed the center of interest in epilepsy research and clinical care, which is also reflected in clinical terminology (ictus, ictal, pre-/post-/peri-ictal).

Previous work has suggested that network dynamics other than seizures (Sz), e.g. spreading depolarization/depression (SD)(*10*), could in principle account for a number of post-ictal symptoms(*2*, *6*, *11*). Most of what is known about SD stems from research on migraine, stroke and traumatic brain injury(*12*–*14*). In this context, Sz and neocortical SD have also been systematically investigated in clinical electrical recordings(*15*–*24*), whereas studies on SD in chronic human epilepsy have remained scarce(*25*, *26*). While SD has been recorded in various brain regions including deep structures like the hippocampus(*27*–*33*), thalamus(*34*, *35*), basal ganglia(*27*), or brainstem(*6*, *7*), the vast majority of SD research has focused on neocortex, which brought about the common term cortical spreading depression (CSD)(*14*). Put simply, SD constitutes a massive ion translocation across the neuronal cell membrane resulting in a profound depolarization

above the inactivation threshold, a break-down of the membrane potential and consecutive neuronal depression(*10*, *14*, *36*). SD can be elicited in various ways, e.g. by energy depletion(*37*–*39*), hypoxia(*11*), high extracellular K^+(*39*–*42*), repetitive electrical or mechanical stimulation(*10*), or optogenetic neuronal depolarization(*43*–*48*). Depending on the etiology, SD has profound effects on affected brain tissue such as transient edema and vasoconstriction, danger molecule release in the extracellular space (i.e. ATP), or immune activation(*11*, *14*, *30*, *49*). Such effects may be reversible, but can also lead to permanent tissue damage(*23*, *50*).

In basic epilepsy research, the role of SD remains debated. SD has both been suggested to increase neural excitability(*33*, *51*), and to disrupt ictal oscillations(*31*, *52*, *53*). Some have speculated about a protective role of SD in epilepsy(*52*, *54*), while others have described Sz-related SD as a potential cause for SUDEP via brain stem invasion(*6*, *7*). Certainly, as most basic research on Sz-related SD has been carried out in vitro, or under anesthesia(*10*, *11*, *27*, *30*, *51*, *52*), the general relationship between Sz-related SD and potentially distinct clinical symptoms have remained understudied. In epileptology, concepts revolving around Sz-related SD and its potential clinical-level impact, aside from SUDEP, currently play little to no role.

Here, we provide evidence in mice and humans that Sz-associated focal spreading depolarization (sSD) constitutes a proper pathoclinical entity in epilepsy. Using two-photon or one-photon widefield imaging (hippocampus, neocortex), field potential and single unit recordings, and behavioral assessment in mice, we first studied seizures during viral encephalitis, and subsequently established an optogenetic approach to

dissociate hippocampal Sz and SD. We find profound region-specific differences in sSD occurrence, characterize its progression, and show that temporomesial SD triggers *post-ictal ambulation* (PIA). Then, by Behnke-Fried (BF) electrode recordings in an initial cohort of four patients with refractory focal epilepsy undergoing pre-surgical diagnostic work-up, we provide corroborating evidence for an increased vulnerability of the human temporomesial system (hippocampus, amygdala) for putative sSD at Sz termination, and differential recovery times of affected vs. non-affected brain regions.

Results

Two-photon Ca^{2+} imaging of epileptic network dynamics during viral encephalitis

We initially set out to study naturally occurring temporal lobe Sz at cellular scale. To this end, we employed resonant two-photon (2p) population Ca^{2+} imaging in the hippocampus (CA1) or cortex (CTX, motor) in awake adult transgenic Thy1-GCaMP6s mice (JAX 025776; 15 Hz scanning, ~700x700 µm, 16X Nikon 0.80 NA 3.0 mm WD) , in the recent Theiler's murine encephalomyelitis virus (TMEV) etiocopy mouse model of TLE (Fig. 1 A, B). The model is based on an initial self-limiting viral encephalitis that encompasses acute disease stage focal onset seizures (~2-7 days post infection [p.i.], Fig. 1 C, Suppl. Fig. 1, for details, see methods)(*55*).

For electrophysiological reference of optically recorded network dynamics, we combined 2p-imaging with local field potential (LFP) recordings (Fig. 1 A, insulated tungsten Ø ~125 µm). Notably, both in bi-hippocampal wireless LFP recordings (Suppl. Fig. 2) and all combined imaging-LFP recordings in CA1 (Fig. 1 E i), focal electrographic Sz were faithfully detected in both hemispheres. Thus, for practical procedural reasons, in experiments involving both chronic in vivo 2p-imaging and LFP recordings, we placed

one LFP electrode at the stereotaxic site of hippocampal TMEV inoculation (from Bregma: AP -1.9, ML 1.6, DV 1.5 mm from pial surface), while imaging was performed in contralateral CA1 or CTX (Fig. 1 A, E). In our framework, electrographic and optical hippocampal Sz corresponded well, while optical neocortical Sz invasion occurred with a delay of seconds (Fig. 1 E ii, 10.20 ± 5.55 sec s.e.m.).

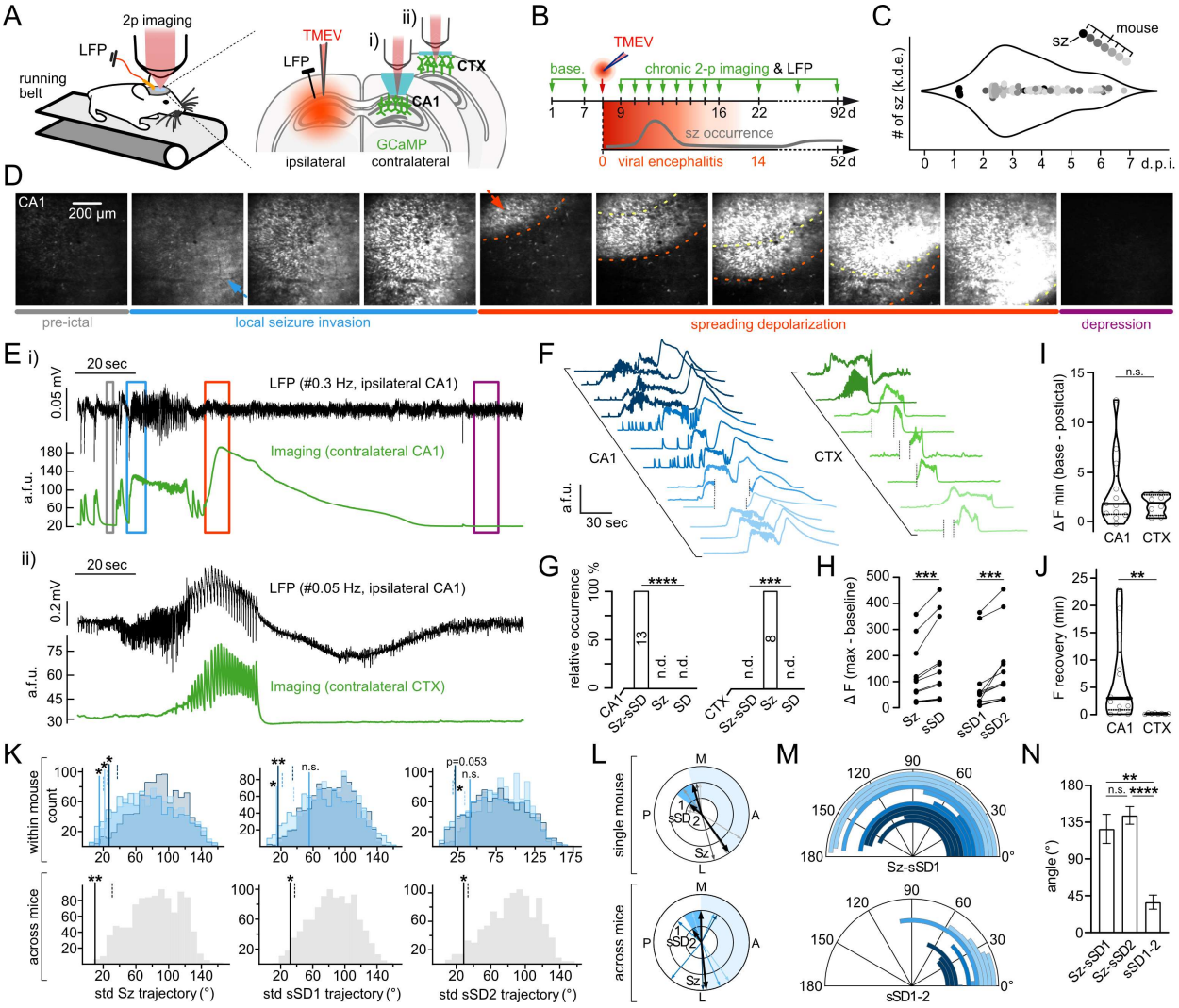

Fig. 1. Chronic hippocampal or neocortical 2p-imaging of seizures during viral encephalitis
A, Exp. setup. Contralateral (contra) cranial window above hippocampus (i: CA1) or neocortex (ii: CTX) to ipsilateral (ipsi) LFP electrode (black pin, at superficial CA1) and TMEV injection site (CA1), in transgenic GCaMP6s mice. **B**, Exp. workflow. **C**, Detected clinical seizures (Sz, filled circles) during viral encephalitis in initial video-monitoring (7 mice, gray shades). Max. number (#) of Sz (k.d.e.: kernel density estimate) typically occur on day 2-5 post injection (d.p.i.). **D**, Representative average (avg) fluorescence (F) images of neuronal signals during pre-ictal baseline (gray), Sz (blue) and sSD (red/violet) invasion of CA1. Arrows depict travelling direction of Sz (blue) or sSD (red). Dotted lines depict propagating wavefronts of sSD1

(red) and sSD2 (yellow). **E**, Two paradigmatic experiments, for approach i) or ii) shown in A. LFP (black, ipsi CA1) and avg population Ca^{2+} imaging signals (green, contra) in CA1 (top, approach i), or CTX (bottom, approach ii)) during local Sz and sSD invasion (a.f.u.: arbitrary fluorescent units). Colored boxes correspond to time periods for avg images in D. Note that sSD is not detected in raw LFP when high-pass filter is set too high (#0.3 Hz, top) whereas a large biphasic LFP shift is visible in bottom panel (#0.05 Hz). Note also delayed optical CTX Sz invasion. **F**, All imaged Sz in CA1 (13 Sz, 4 mice, blue shades) or CTX (8 Sz, 3 mice, green shades). Note the presence or absence of sSD. Dotted lines indicate momentary breaks between imaging sessions. **G**, Quantification of occurrence of Sz-sSD, Sz, or SD during encephalitis in CA1 (left, Friedman test, $p<0.0001$) or CTX (right, Friedman test, $p=0.0005$), n.d. = not detected. **H**, Comparison of Sz vs. sSD relative Ca^{2+} signal amplitudes in CA1 (a.f.u., Δ F: Delta Fluorescence), Left: Sz vs sSD, paired Wilcoxon test (12 Sz-sSD, 117.1 ± 32.6 [Sz] vs. 164.8 ± 43.35 [sSD], $p=0.0005$), Right: sSD1 vs sSD2, paired Wilcoxon test (12 sSD1-sSD2, 91.92 ± 36.2 [sSD1] vs. 144.1 ± 40.42 [sSD2], $p=0.0005$). **I**, Comparison of CA1 vs CTX pre- and post-ictal minimal F (a.f.u., Δ F min), Mann-Whitney test (13 events in CA1 vs. 8 events in CTX, 3.02 ± 3.54 vs. 1.77 ± 1.04, $p=0.8044$). **J**, Comparison of CA1 vs CTX F recovery time (minutes), Mann-Whitney test (13 events in CA1 vs. 8 events in CTX, 6.531 ± 2.15 vs. 0.188 ± 0.038, $p=0.0061$). **K**, Observed (solid lines) standard deviations (std) of spatial trajectory angles (°) of Sz (left), sSD1 (middle), and sSD2 (right). Top panel, within-mouse analysis: 3 mice (blue shades, each mouse ≥ 3 imaged Sz-sSD) vs corresponding shuffled distributions from 1000 randomized datasets. Bottom panel, across-mice analysis: solid line depicts observed std of angle means (all 4 CA1-imaged mice) vs corresponding shuffled distributions from 1000 randomized datasets (gray). In all plots, dashed lines mark respective significance thresholds (where observed std <95% of all surrogate std). **L**, Top: Paradigmatic experiment with spatial Sz-sSD trajectory map within imaged FOV (general anatomical landmarks: M medial, L lateral, P posterior, A anterior). Outer ring shows Sz, intermediate ring sSD1, inner ring sSD2 trajectories (gray shades: individual events, black: mean). Bottom: Across-mice depiction (blue shades: per-mouse angle mean, black: grand mean) for Sz, sSD1 and sSD2. Top and bottom: shaded areas display mean trajectory angle between Sz and sSD1 (light blue), or sSD1 and sSD2 (dark blue). **M**, Calculated angles (°) for each imaged Sz-sSD1 and sSD1-sSD2 (blue shades for individual mice). One event excluded from analysis, as immediate Sz onset was not recorded, see Fig. 1 F. **L**, Quantification of angles (°) between Sz and sSD1 (12 events, 126.9 ± 17.87), Sz and sSD2 (11 events, 143.4 ± 10.77), and sSD1 and sSD2 (12 events, 37.23 ± 8.65), mixed effects analysis with Tukey's test ($F[1.396, 13.96]=26.35$; Sz-sSD1 vs. Sz-sSD2 $p=0.3938$, Sz-sSD1 vs. sSD1-2 $p=0.0020$, Sz-sSD2 vs. sSD1-2 $p<0.0001$). For entire fig.: Plotted error bars represent s.e.m., all given $\pm$ denote s.e.m.. Depiction of violin plots: median (solid lines), quartiles (dotted lines). Depiction of statistical significance: n.s. not significant, *$p < 0.05$, **$p < 0.01$, ***$p < 0.001$, ****$p < 0.0001$.

Consistent association of seizures with spreading depolarization in hippocampus

Across a total of 205 imaging hours (CA1: 118 hrs; CTX: 87 hrs) in 26 mice and 158 days of viral encephalitis, interictal epileptiform network activity was detected in all mice. In 7 out of those 26 mice, based on the ACNS consensus criteria for ictal activity(*56*)(for details, see methods), we successfully captured seizures (13 Sz in CA1, 4 mice [Fig. 1 F, blue/left], 8 Sz in CTX, 3 mice [Fig. 1 F, green/right]). Strikingly, imaged hippocampal Sz in CA1 were consistently followed by a massive second, multiplexed wave of Ca^{2+} signal, in what appeared to be spreading depolarization / depression (SD, Fig. 1 F, G and suppl.

movie 1)(*57*). Typically, two Sz-associated SD waves (sSD1 and sSD2, Fig. 1 D) succeeded one another in the imaged field of view (12 sSD1-sSD2, delay: 6.044 ± 0.9156 sec). In line with the published literature, both sSD waves progressed at the speed of few mm/min across the imaged CA1 region, while preceding Sz propagated much faster (13 sSD1: 7.75 ± 0.52, 12 sSD2: 6.87 ± 0.36, 12 Sz: 79.6 ± 12.67 mm/min; One-way ANOVA with Tukey's test ($F[2,34]=30.56$; sSD1 vs. sSD2 $p=0.8823$, sSD1 vs. Sz $p<0.0001$, sSD2 vs. Sz $p<0.0001$). In CA1, neither Sz nor SD ever occurred alone. By contrast, in the imaged CTX, isolated SD or sSD were never detected (Fig. 1 F, G, suppl. movie 2). As described previously, maximum hippocampal Ca^{2+} signal amplitudes of Sz-related SD (sSD) were consistently larger than preceding Sz (Fig. 1 H left)(*9*). Moreover, sSD2 showed consistently larger amplitudes than sSD1 (Fig. 1 H right). Intriguingly, despite the clear discrepancy of sSD occurrence in CA1 versus CTX, both recorded territories displayed reduced basic Ca^{2+} fluorescence post-sSD (CA1) or post-Sz (CTX) in comparison to the pre-ictal period (Fig. 1 I). However, recovery times to pre-ictal basic Ca^{2+} fluorescence in CA1 were longer than in CTX, on the order of minutes (Fig. 1 J).

Hippocampal seizures and sSD propagate in opposite directions

To evaluate potentially conserved micro-progression patterns in naturally occurring hippocampal Sz and sSD during encephalitis, we analyzed spatiotemporal Sz and sSD trajectories across successive events similarly to previous reports(*58*, *59*). Based on the recruitment timepoints of identified individual neurons for a given Sz or sSD, we calculated interpolated linear spatial trajectories of every Sz or sSD across events in all CA-1 imaged mice (Fig. 1 F). Along the antero-posterior and medio-lateral dimension of the imaged field of view (FOV), this resulted in a number of spatial vectors per Sz, sSD1

and sSD2. For within-mouse analysis (Fig. 1 K, top panel), we calculated the standard deviations (std) across spatial vectors for Sz, sSD1 and sSD2 for each mouse with at least three recorded events where Sz and sSD onsets were fully captured (3 mice, CA1, 3.3 ± 0.3 events s.e.m., Fig. 1 F). Since chance level trajectory std's are unknown, the derived standard deviations of observed trajectories were compared to randomized surrogate distributions. In all three mice, Sz trajectories displayed significantly smaller variability in the observed dataset than would be expected by chance (Fig. 1 K top left) suggesting repeated spatiotemporal Sz progression pathways(*58*–*60*). To a lesser extent, the same held true for sSD waves (Fig. 1 K top middle, right). A subsequent analysis across mice (std of per-experiment means) showed significantly small trajectory std's for Sz, sSD1 and sSD2 (Fig. 1 K bottom), which suggested, beyond patterned progression within experiments, commonly repeated micro-progression routes of Sz and sSD.

Next, we investigated the relative spatial relationship between individual Sz and successive sSD in CA1 by calculating the angles between spatial trajectories of Sz and sSD1 as well as sSD1 and sSD2 (Fig. 1 L). Unexpectedly, we found vast angles between Sz and sSD1 trajectories (Fig. 1 L-N). Typically, in our CA1 FOV, Sz progressed along a medio-lateral path (hippocampal anatomy: distoproximal path, towards CA2 (*61*)), while sSD1/2 travelled the opposite way (proximodistal path, from CA2; Fig. 1 L, M top panel, N: 4 mice, 12 Sz-sSD1 events, median angle 162.01° [range 42.1 – 177.2°]). By contrast, sSD1 and sSD2 displayed more similar spatial trajectories (Fig. 1 L, M bottom panel, N: 4 mice, 11 sSD1-sSD2 events, median angle 42.5° [0.1 – 100.5°]).

Together, these experiments identified a complete association of naturally occurring Sz and sSD in CA1 during viral encephalitis, whereas this association was not found in the imaged CTX. Regardless, both CA1 and CTX displayed reduced basic fluorescence post-

sSD or post-Sz, but the post-sSD recovery time of the neuronal network in CA1 clearly outlasted the post-Sz recovery time in CTX. Sz and sSD waves showed significantly non-random spatiotemporal progression, while strikingly, hippocampal Sz and sSD1 travelled in vastly different directions (Sz: CA1 → CA2, sSD: CA2 → CA1).

Post-ictal ambulation **is associated with sSD in hippocampus**

In the TMEV model, we went on to correlate the observed network dynamics to clinical signs (semiology) related to Sz or sSD. Importantly, during 2p-imaging of focal Sz in awake head-restrained mice, generalized tonic-clonic convulsions never occurred.

What stood out at the clinical level in encephalitis-related Sz was that the mice regularly started locomoting upon optical sSD appearance, which then lasted for minutes (Fig. 2 A, Suppl. Fig. 3). In comparison to the pre-ictal period, locomotion was indeed systematically increased post-sSD (pre-ictal 5min vs. post-sSD 5min, Fig. 2 B), fitting well with so-called *post-ictal wandering* (PIW), a prominent post-ictal symptom regularly encountered in clinical epileptology (see also discussion). PIW is most frequently observed in patients with TLE(*3*, *4*), and characterized by unconscious ambulatory automatisms. It typically lasts for minutes to hours, with potentially life-threatening consequences (e.g. if one walks onto a highway). Aside from locomotion time, we quantified travelled distance, number of locomotion episodes and maximum locomotion speed, all of which were increased over the 5 min post-sSD period as well (Fig. 2 C-E). Together, these experiments showed that during viral encephalitis, hippocampal sSD is associated with the onset of a locomotor phenotype that lasts for minutes, providing a candidate mechanism for PIW. Throughout this text, we refer to this locomotor phenotype in mice as *post-ictal ambulation* (PIA).

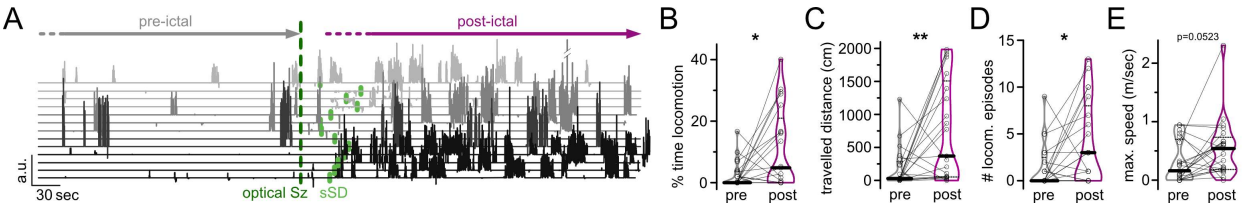

Fig. 2. Hippocampal sSD during encephalitis corresponds to onset of post-ictal ambulation
A, Locomotion on linear treadmill across 13 Sz-sSD events in all 4 CA1-imaged mice (gray shades) during encephalitis, aligned by optical Sz invasion (dotted green line), sSD onsets marked in light green. **B-E**: Comparison of 21 pre- vs. post-ictal periods (5min each) in all imaged 7 mice (CA1 or CTX). **B**, % time locomotion, paired t-test (2.525 ± 0.957 [pre] vs. 11.06 ± 2.83 [post], p=0.0119). **C**, Travelled distance (cm), paired t-test (184.1 ± 67.32 [pre] vs. 754.3 ± 166.5 [post], p=0.0065). **D**, # of locomotion episodes, paired t-test (1.429 ± 0.519 [pre] vs. 4.0 ± 0.974 [post], p=0.0239). **E**, maximum speed (m/sec), paired t-test (0.312 ± 0.077 [pre] vs. 0.553 ± 0.11 [post], p=0.0523). For entire fig.: All given ± denote s.e.m.. Depiction of violin plots: median (solid lines), quartiles (dotted lines). Depiction of statistical significance: n.s. not significant, *p < 0.05, **p < 0.01, ***p < 0.001, ****p < 0.0001.

Optogenetic dissection of the role of hippocampal SD in *post-ictal ambulation*

Although hippocampal sSD appearance coincided with the onset of sustained locomotion during encephalitis, the complete association of hippocampal Sz and sSD precluded us from decisively differentiating the role of Sz versus SD in PIA. To arrive at a more mechanistic understanding, based on previous studies(*62*, *63*), we established a combined 2p-imaging (GCaMP6s [JAX 025776], or jRGECO [AAV2/1-NES-jRGECO1a] Vector Core Uni Bonn), 1p optogenetics (ChR2, AAV-hSyn-hChR2[H134R]-mCherry, Addgene ID 26976-AAV5) and LFP approach (Fig. 3 A left; 3 B, suppl. Fig. 4) that allowed us to generate either Sz or SD in a controlled manner. Using this 2p/1p/LFP approach, Sz or SD were never elicited by 2p-imaging itself (16X Nikon 0.80 NA, wavelength range 940-980nm [GCaMP] or 1050nm [jRGECO]).

In CA1, Sz could be reliably elicited by a brief square wave light pulse (typically 500-750ms, Coherent Inc., CA, Sapphire LP CW laser, 488nm, power at brain surface 4-5mW/mm^2) in the imaged FOV (Fig. 3 C left, D). Interestingly, these optogenetically induced Sz in the healthy hippocampus were again consistently followed by sSD, and Sz-

sSD could be bilaterally detected (Fig. 3 C left, D, suppl. movie 3). To reliably trigger isolated SD without a preceding focal Sz, a prolonged light pulse (~4 sec, 488nm, 4-5mW/mm^2) was applied, similarly to previous reports (Fig. 3 C right, suppl. Fig. 4 C, suppl. movies 4, 5)(*44*, *45*). Neither Sz nor SD were elicited by control illumination at 561nm (Coherent Inc., Santa Clara, CA, Sapphire LP CW laser, 7 mW/mm^2), ensuring that the effects were not unselectively driven by light stimulation alone. Notably, hippocampal encephalitic Sz-sSD and optogenetic Sz-sSD showed similar differential optical signal amplitudes (Suppl. Fig. 5 A). Further, there were no significant differences between optogenetic sSD vs. SD depolarization half-widths and progression speeds in the optical recordings (suppl. Fig. 5 B, C). In keeping with the results during encephalitis, imaged CA1 also consistently displayed reduced basic Ca^{2+} fluorescence in the wake of optogenetic SD or Sz-sSD as compared to the pre-stimulation period (Suppl. Fig. 5 D), and fluorescence recovery times occurred on the order of minutes (Suppl. Fig. 5 E). Thus, basic SD features were preserved across different experimental models.

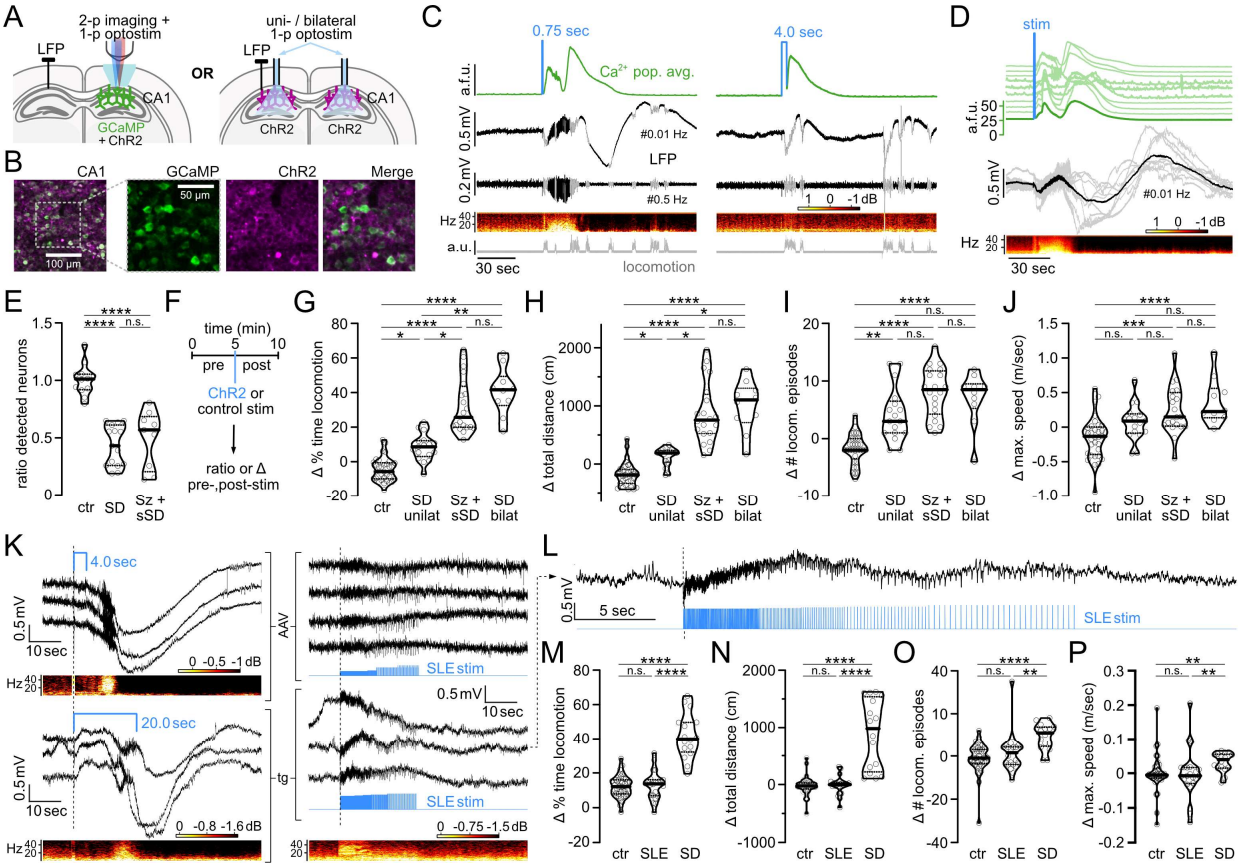

Fig. 3. Optogenetic dissection of hippocampal SD vs. SLE in post-ictal ambulation

A, Optogenetic experimental setup. Left (2p/1p/LFP approach): CA1 window for 2p imaging (GCaMP6s or jRGECO1a) and 1p optogenetic stimulation (ChR2: 488nm, ctr: 561nm), both contralateral to LFP electrode (black pin, at CA1). Right (1p/LFP approach): uni-/bilateral optogenetic stimulation (ChR2: 475nm, ctr: 590nm) via optical cannulae (CA1) and LFP electrode (black pin, at CA1). **B**, Co-expression of GCaMP6s (transgenic, green) and ChR2 (AAV, magenta) in CA1 (str. pyr.). **C**, Two examples for 2p/1p/LFP approach, Left: 0.75 sec optogenetic stimulation (488 nm) elicits Sz-sSD (optical ipsilateral, electrographic contralateral, note differential Sz-sSD delays). Top trace depicts avg pop. Ca^{2+} signal, middle traces LFP (0.01-50 Hz or 0.5-50 Hz) and corresponding spectrogram, bottom trace locomotion; locomotion artifacts in LFP are marked gray in LFP traces; Right: same setting, but 4 sec optogenetic stimulation triggers isolated SD in imaged field of view. In contralat. LFP, neither Sz nor SD are detected. Locomotion artefacts marked in gray in LFP traces. **D**, All 2p/1p/LFP optogenetic Sz stim. (3 mice, 9 Sz-sSD [3 each]). Top: avg. Ca^{2+} population signals per stim. (light green), avg. signal across stim. below (green). Bottom: Superimposed individual LFP traces (gray, 0.01-50 Hz) with avg. LFP (black), and corresponding avg. spectrogram. All optogenetic Sz were followed by sSD. Note the pronounced post-sSD spectral depression. **E**, Ratio of detectable neurons in imaged FOV (CA1) across pre- and post-stim. periods (5min each) in 5 mice, pooled sample #: 12 ctr stim., 15 SD and 9 Sz-sSD, pre/post ratio: 1.006 ± 0.0396 (ctr), 0.433 ± 0.046 (SD), 49.33 ± 0.083 (Sz-sSD). One-way ANOVA with Tukey's test (F [2, 33] = 35.37; ctr vs SD p<0.0001, ctr vs Sz-sSD p<0.0001, SD vs. Sz-sSD p=0.7265. **F**, Optogenetic stim. framework for analysis in G to J. **G-J**, Comparison of respective value Δ between pre- and post-stim. periods (5min each) in 7 mice (1p/LFP approach), pooled sample #: 33 ctr stim., 17 unilateral SD, 20 Sz-sSD, 10 bilateral SD. **G**, Δ % time locomotion: -4.403 ± 1.187 (ctr), 8.331 ± 1.861 (unilat. SD), 32.18 ± 3.540 (Sz-sSD), 40.68 ± 4.325 (bilat. SD). One-way ANOVA with Tukey's test (F[3,76]=72.44; ctr vs unilat. SD p=0.001, ctr vs Sz-sSD p<0.0001, ctr vs. bilat. SD p<0.0001, unilat. SD vs. Sz-sSD p<0.0001, unilat. SD vs. bilat. SD p<0.0001, Sz-sSD vs. bilat. SD p=0.1862). **H**, Δ travelled distance (cm): -177.4 ± 35.15 (ctr), 129.3 ± 37.64 (unilat. SD), 874.3 ± 116.9 (Sz-sSD), 1001.0 ± 139.0 (bilat. SD). One-way ANOVA with Tukey's test (F[3, 76]=57.39; ctr vs unilat. SD p=0.0188, ctr vs Sz-sSD p<0.0001, ctr vs. bilat. SD p<0.0001, unilat. SD vs. Sz-sSD p<0.0001, unilat.

SD vs. bilat. SD p<0.0001, Sz-sSD vs. bilat. SD p=0.9120). **I**, Δ # of locomotion episodes: -1.697 ± 0.4636 (ctr), 4.176 ± 1.129 (unilat. SD), 8.05 ± 0.95 (Sz-sSD), 7.0 ± 1.461 (bilat. SD). One-way ANOVA with Tukey's test (F[3, 76]=32.48; ctr vs unilat. SD p<0.0001, ctr vs Sz-sSD p<0.0001, ctr vs. bilat. SD p<0.0001, unilat. SD vs. Sz-sSD p=0.0152, unilat. SD vs. bilat. SD p=0.2561, Sz-sSD vs. bilat. SD p=0.8929). **J**, Δ maximum speed (m/sec): -0.1516 ± 0.0523 (ctr), 0.072 ± 0.063 (unilat. SD), 0.243 ± 0.077 (Sz-sSD), 0.366 ± 0.106 (bilat. SD). One-way ANOVA with Tukey's test (F[3, 76]=10.80; ctr vs unilat. SD p=0.0803, ctr vs Sz-sSD p=0.0001, ctr vs. bilat. SD p<0.0001, unilat. SD vs. Sz-sSD p=0.3423, unilat. SD vs. bilat. SD p=0.0876, Sz-sSD vs. bilat. SD p=0.7322). **K**, Bilateral optogenetic (1p/LFP approach [0.05-50 Hz]) SD vs. Sz-like episodes (SLE, for details see methods). Displayed are two exp. in adult animals, one mouse with AAV-ChR2 (top), one transgenic (tg) thy1-ChR mouse (bottom). In both approaches, bilateral hippocampal stim. (CA1; 475nm, respective stim. patterns in blue) reliably elicited either SD (left LFP panels with corresponding avg. spectrogram), or isolated SLE (right LFP panels with corresponding avg. spectrogram). Corresponding control stim. (590nm) neither elicited SD nor SLE regardless of stim. pattern (suppl. Fig. 8). **L**, Magnified individual optogenetic SLE from K (dotted arrow; LFP in black, stim pattern in blue). Note close LFP correspondence to stim. pattern, with successive frequency decrement and amplitude increment across SLE. **M-P**, Comparison of respective value Δ between pre- and post-stim. (1p/LFP approach, all stim. bilateral) periods (5min each) in 6 mice (3 AAV, 3 tg), pooled sample #: 37 ctr, 22 SLE, 16 SD. **M**, Δ % time locomotion: -1.337 ± 1.234 (ctr), -0.4183 ± 2.077 (SLE), 33.85 ± 3.959 (SD). One-way ANOVA with Tukey's test (F[2,72]=70.71; ctr vs SLE p=0.9424, ctr vs SD p<0.0001, SLE vs. SD p<0.0001). **N**, Δ travelled distance (cm): -22.81 ± 26.14 (ctr), -13.25 ± 33.43 (SLE), 885.7 ± 152.3 (SD). Kruskal-Wallis with Dunn's test (ctr vs SLE p>0.9999, ctr vs SD p<0.0001, SLE vs. SD p<0.0001). **O**, Δ # of locomotion episodes: -0.973 ± 1.169 (ctr), 1.545 ± 1.939 (SLE), 9.25 ± 1.561 (SD). Kruskal-Wallis with Dunn's test (ctr vs SLE p>0.9999, ctr vs SD p<0.0001, SLE vs. SD p=0.0016). **P**, Δ maximum speed (m/sec): 0.04196 ± 0.8761 (ctr), -0.2461 ± 1.537 (SLE), 3.251 ± 0.6887 (SD). Kruskal-Wallis with Dunn's test (ctr vs SLE p>0.9999, ctr vs SD p=0.0083, SLE vs. SD p=0.0079). For entire fig.: All given ± denote s.e.m.. Depiction of violin plots: median (solid lines), quartiles (dotted lines). Depiction of statistical significance: n.s. not significant, *p < 0.05, **p < 0.01, ***p < 0.001, ****p < 0.0001.

In line with our imaging experiments during encephalitis, both optogenetically triggered Sz-sSD and isolated SD led to an equally strong post-ictal reduction of detectable neurons in the FOV (Fig. 3 E) underscoring functional depression of the CA1 network due to SD. To make sure that these optical imaging results were not confounded by GFP-quenching due to SD-related pH shifts (ongoing neuronal firing in the quenched absence of optical signals), we repeated the optogenetic SD experiments with electrophysiology, now employing hippocampal tetrode recordings (+ optical cannula, see methods) in freely moving mice instead of 2p-imaging. In keeping with the imaging experiments, we found a prolonged and profound cessation of firing of a large majority of units upon optogenetic SD in CA1 (suppl. Fig. 5 F), and increased post-SD ambulation (suppl. Fig. 5 G, H).

As unilateral optogenetic Sz induction consistently triggered bi-hippocampal Sz (Fig. 3 C left, D), we additionally implemented a 1p optogenetic stimulation approach enabling uni- or bilateral hippocampal Sz or SD induction via implanted optical cannulas, combined with LFP recordings (1p/LFP approach; Fig. 3 A right). Here, for optogenetic Sz or SD induction versus control, instead of lasers, fiber-coupled LEDs were employed using the same stimulation durations as mentioned above (Chrolis/Thorlabs: 475 nm or 590nm [2-3mW/mm^2]). Based on the 2p/1p/LFP or 1p/LFP approach, we then compared a pre- and post-stimulation (for control and SD) or pre-stimulation and post-sSD (for Sz-sSD) period (5min each, Fig. 3 F) analyzing the same locomotor parameters as in encephalitis (Fig. 2 B-E).

In the initial 2p/1p/LFP experiment, we unilaterally triggered SD or Sz versus unilateral control (Suppl. Fig. 6 A-D). In the 1p/LFP experiment, we carried out bilateral SD, unilateral Sz (except in one animal, where bilateral stimulation was necessary to trigger hippocampal Sz), and uni- or bilateral control stimulations (Suppl. Fig. 6 E-H). Since with respect to all analyzed clinical parameters, uni- versus bilateral control stimulations showed no significant differences, neither within nor across experimental configurations (Suppl. Fig. 6 E-L), these data were pooled. As the same held true for uni- and bilateral hippocampal Sz inductions within and across experiments, these data were also pooled (Suppl. Fig. 6 I-L, statistics for suppl. Fig. 6 are displayed in suppl. Table 1 and 2).

Remarkably, in comparison to control (590nm stim.), isolated optogenetic unilateral SD (475nm stim.) in CA1 produced an increased locomotor phenotype like Sz-sSD in CA1 during encephalitis, indicating that hippocampal SD alone is sufficient to trigger PIA (Fig. 3 G-J, suppl. Fig. 7, suppl. Fig. 5 G, H) across experimental frameworks (2p/1p/LFP, tetrode/1p/LFP, 1p/LFP). Interestingly, across most tested locomotor parameters (% time

362 of locomotion, travelled distance, number of locomotion episodes), the effect triggered by
363 unilateral hippocampal optogenetic SD stimulation was significantly surpassed by
364 unilateral hippocampal optogenetic Sz-sSD stimulation (Fig. 2 G-J, suppl. Fig. 7). We
365 hypothesized that this difference in effect size could be due to the involvement of bilateral
366 hippocampal circuitry during focal onset hippocampal Sz, which we had observed during
367 encephalitis and optogenetic experiments (Fig. 1 E, 3 C left). In this case, even a
368 unilaterally triggered hippocampal Sz would, due to its bi-hippocampal recruitment,
369 prompt bilateral hippocampal sSD (Fig. 3 C left). In turn, unlike hippocampal Sz-sSD, due
370 to the different, non-synaptic nearest-neighbor progression of SD, unilaterally triggered
371 SD would typically remain unilateral (Fig. 3 C right). In line with this rationale, uni- or
372 bilateral hippocampal Sz-sSD stimulation produced a similar locomotor phenotype
373 (Suppl. Fig. 6 E-H), and Sz-sSD stimulation systematically produced a stronger
374 phenotype as compared to unilateral optogenetic SD stimulation, except for maximum
375 speed (Fig. 3 G-J, suppl. Fig. 6 A-D and I-L). Yet crucially, Sz-sSD and bilateral SD
376 stimulation consistently evoked a similar clinical phenotype across analyzed locomotor
377 parameters (Fig. 3 G-J, suppl. Fig. 6 E-L, suppl. Fig. 7).
378 To further substantiate the evidence that hippocampal SD is a primary driver of PIA, one
379 would need to show that isolated hippocampal Sz fail to trigger PIA, which proved
380 experimentally impossible in our experiments thus far (100% association of SD with
381 encephalitic or optogenetic hippocampal Sz). For several reasons including unclear site
382 of sSD origin and currently insufficiently known technical means to precisely inhibit
383 propagating sSD (see discussion), we thus set out to implement an experiment within our
384 optogenetic in vivo framework that allows to produce hippocampal Sz-like episodes (SLE)
385 without subsequent SD. To this end, using our 1P/LFP approach (Fig. 3 A right), we

titrated custom optogenetic SLE vs. SD in mice with AAV-mediated hippocampal ChR2-expression, or transgenic (tg) thy-ChR2 mice (B6.Cg-Tg(Thy1-COP4/EYFP)18Gfng/J, JAX 007612). SLE stimulations were designed such that they match the average duration of all optogenetic Sz (27 Sz [electr./opt. pooled]: 24.63 ± 1.509 sec; SLE stim.: 22 SLE [electr.]: 25 ± 0.335 sec), and based on ACNS consensus criteria for ictal EEG activity including rhythmic activity (>2.5Hz), frequency decrement and amplitude increment (Fig. 3 K right, L; Suppl. Fig 8 B-D [stim. parameters], for details, see methods). In both groups (AAV, TG), bilateral SLE or SD could be reliably triggered in CA1 (475nm, Fig. 3 K, L), whereas matching control stimulation (560nm) never produced SLE or SD (Suppl. Fig. 8 A). Then, we analyzed pre- vs. post-stim. ambulation as before (Fig. 3 F-J). Since there were no differences between any of the employed control stimulation paradigms with regards to all analyzed locomotor parameters (Suppl. Fig. 8 E-H), these control groups were pooled. Remarkably, across all analyzed locomotor parameters, while bi-hippocampal SD produced PIA as in our prior optogenetic experiments, optogenetic bi-hippocampal SLE never deviated significantly from controls (Fig. 3 M-P). Together, these experiments unveiled i) a mechanistic role of hippocampal SD in PIA, ii) a scaling of severity of the clinical phenotype depending on uni- vs. bilateral hippocampal SD, and iii) similar clinical effect sizes across hippocampal Sz-sSD and bilateral SD. Importantly, optogenetic hippocampal SLE failed to trigger PIA. This suggests that rather than hippocampal Sz themselves, SD prompts PIA.

Optogenetic induction of hippocampal SD and neocortical widefield imaging

While we had never observed Sz-sSD in motor cortex using 2p-imaging during encephalitis, our imaged FOV was confined to ~700x700 µm. Thus next, with the

optogenetic approach of on-demand focal SD induction at hand, and combined LFP recordings and one-photon (1p) widefield Ca^{2+} imaging, we went on to investigate the potential spread of optogenetic unilateral hippocampal SD to CTX(*32*, *33*). For hemispheric neocortical 1p-imaging (30 Hz scanning, 470 / 405 nm, LED M470L3 / M405L3, Thorlabs) through cleared skull in awake adult mice, we employed an inverted tandem lens macroscope(*64*), and transgenic tetO-GCaMP6s / CaMK2a-tTA mice (JAX 024742 / 007004) expressing GCaMP6s in excitatory neurons across cortical layers (for details, see methods) (Fig. 4 A).

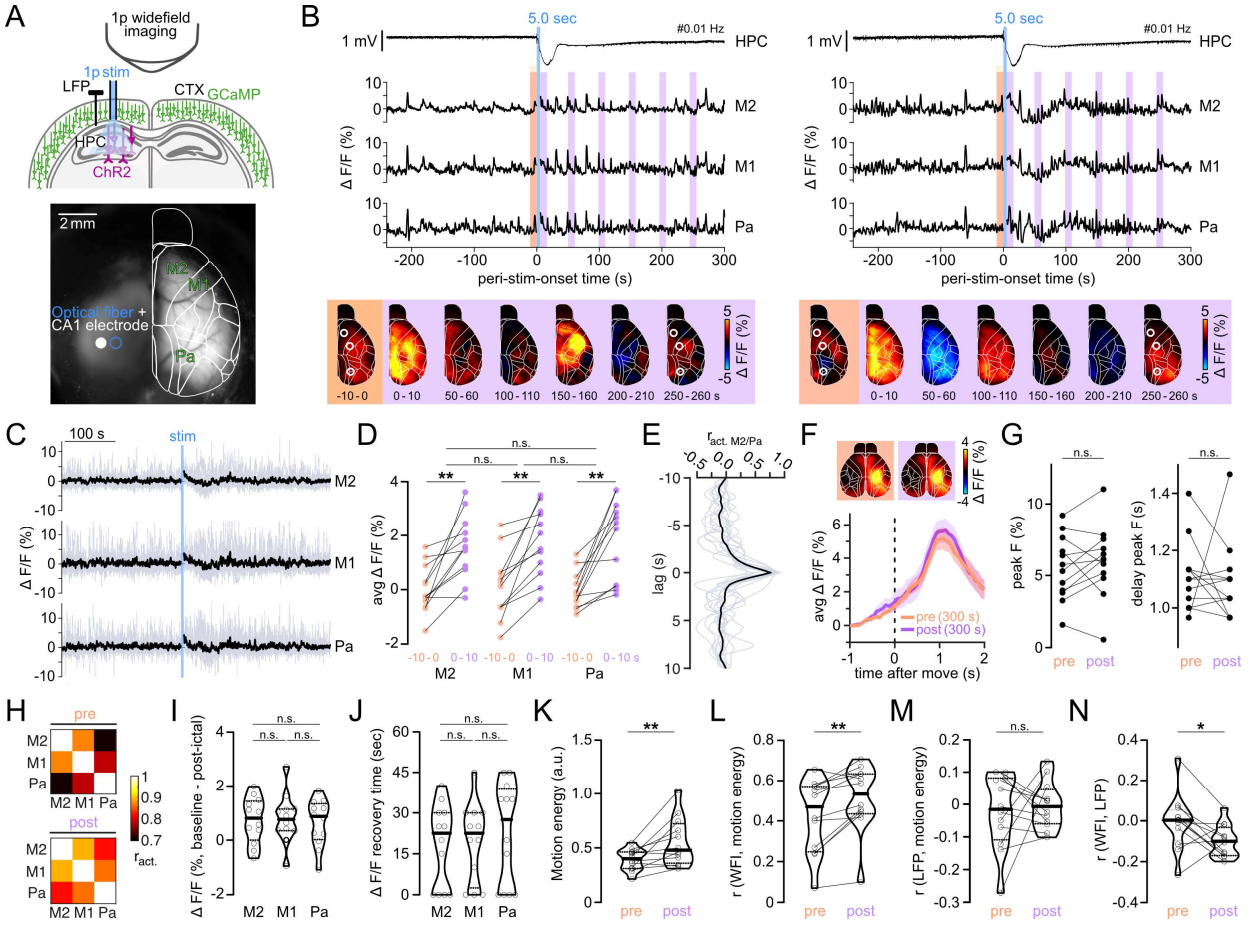

Fig. 4. Hippocampal SD coactivates but does not invade imaged neocortex
A, Top: Experimental setup, widefield Ca^{2+} imaging of neocortex (CTX) in tetO-GCaMP6s/CaMK2a-tTA mice through cleared skull, in combination with hippocampal optogenetic 1p stimulation (ChR2, optical cannula at CA1) and LFP (black pin, at CA1), Bottom: Example image of cortical surface after skull clearing, and implant sites of LFP electrode (white filled circle) and optical fiber (blue circle). Overlaid white lines show Allen CCF borders. **B**, Two examples of stimulus-related CTX activity. Hippocampal (HPC) LFP of

optogenetic SD stimulation (5 sec, blue line), and cortical widefield Ca^{2+} activity in secondary/primary motor (M2, M1) and parietal cortex (P). Corresponding to pre- (orange) and post-stim. periods (violet) 10-sec avg Δ F/F images of CTX activity (bottom, white circles depict M2, M1, P). Note immediate post-stim. widefield CTX activation and continued post-stim. activity, either without any baseline F shift (left) or a brief transient negative baseline shift (right), yet always with continued presence of cortical Ca^{2+} transients. **C**, Superposition of peri-stim. CTX Δ F/F activity traces (individual traces in gray, mean in black; 3 mice, 12 HPC SD stim. [4/mouse, 1/day]). **D**, Quantification of pre- (-10 - 0 sec to stim., orange) vs. post-stim. (0 – 10 sec from stim., violet) avg CTX activity in M2 (0.01 $\pm$ 0.252 [pre] vs. 1.589 $\pm$ 0.337 [post]), M1 (0.118 $\pm$ 0.348 [pre] vs. 1.778 $\pm$ 0.371 [post]) and P (-0.044 $\pm$ 0.196 [pre] vs. 1.831 $\pm$ 0.432 [post]). One-way ANOVA with Šidák's test (F[2.146, 23.60] = 17.98; pre vs. post: M2 p=0.0029, M1 p=0.0014, P p=0.0018). No significant differences of Δ (post – pre) activity among M2, M1, and P. One-way ANOVA with Tukey's test (F[1.837, 20.21]=0.5231; M2 vs. M1 p=0.946, M2 vs. P p=0.657, M1 vs. P p=0.766). **E**, Cross-correlation of peri-stim. activity of M2 and P (12 HPC SD stim., [4/mouse, 1/day], individual traces in gray, mean in black), mean lag = 0 sec. **F-N**, 'pre' and 'post' denote pre- vs. post-stim. periods of 5min each. All quantifications include 3 mice and 12 HPC SD stim.. **F**, Top: avg Δ F/F images of movement-related CTX Ca^{2+} transients. Bottom: corresponding movement-related avg Δ F/F CTX Ca^{2+} dynamics (shades depict s.e.m.). Note congruence btw. pre- (orange) vs. post-stim. (violet) period (pre vs. post events). **G**, Quantification of pre- vs. post-stim. post-movement-onset Ca^{2+} dynamics shown in F. Left: avg. peak Δ F/F post-movement-onset (3 mice, 12 HPC SD stim.). Paired t-test (5.532 $\pm$ 0.6456 [pre] vs. 6.002 $\pm$ 0.7225 [post], p=0.3639). Right: avg. delay (sec) of peak Δ F/F post-movement-onset. Wilcoxon test (1.111 $\pm$ 0.035 [pre] vs. 1.092 $\pm$ 0.04 [post], p=0.4336). **H**, Pre- and post-stim. activity correlation of M2, M1, and P. Note increased correlation of activity post HPC SD stimulation. **I**, CTX pre- vs. post-ictal minimal F (Δ min F baseline/min F post-ictal; M2 0.739 $\pm$ 0.243, M1 0.781 $\pm$ 0.26, P 0.643 $\pm$ 0.247), One-way ANOVA with Tukey's test (F[2, 33]=0.0807; M2 vs. M1 p=0.992, M2 vs. P p=0.96, M1 vs. P p=0.919). Note that all areas show a decreased post-stim. min F on avg. **J**, Comparison of cross-area F recovery time (sec, M2 18.33 $\pm$ 4.323, M1 19.58 $\pm$ 4.15, P 22.5 $\pm$ 5.418), One-way ANOVA with Tukey's test (F[2, 33]=0.2102; M2 vs. M1 p=0.98, M2 vs. P p=0.804, M1 vs. P p=0.898). **K**, Quantification of pre- vs. post-stim avg. motion energy (a.u.: arbitrary units). Paired t-test (0.3916 $\pm$ 0.02803 [pre] vs. 0.5545 $\pm$ 0.0643 [post], p=0.009). **L**, Correlation of wide-field imaging (WFI) and motion energy, pre- vs. post-stim. Paired t-test (0.424 $\pm$ 0.05273 [pre] vs. 0.5140 $\pm$ 0.0479 [post], p=0.0023). **M**, Correlation of LFP and motion energy, pre- vs. post-stim. Paired t-test (-0.0233 $\pm$ 0.0331 [pre] vs. -0.0029 $\pm$ 0.021 [post], p=0.6402). **N**, Correlation of wide-field imaging (WFI) and LFP, pre- vs. post-stim. Paired t-test (-0.0059 $\pm$ 0.040 [pre] vs. -0.0991 $\pm$ 0.0791 [post], p=0.0367). For entire fig.: All given $\pm$ denote s.e.m.. Depiction of violin plots: median (solid lines), quartiles (dotted lines). Depiction of statistical significance: n.s. not significant, *p < 0.05, **p < 0.01, ***p < 0.001, ****p < 0.0001.

Around six weeks before the actual experiment, pAAV-hSyn-hChR2(H134R)-mCherry was stereotactically injected into the left hippocampal CA1 region (coordinates from Bregma: AP -1.9, ML -1.6, DV -1.5 mm). In addition, a custom-made optrode comprising an insulated tungsten electrode (Ø ~125 µm) and an optical fiber (Ø 200 µm, NA = 0.37) were chronically implanted above the left hippocampus, for LFP recordings and optical stimulation.

Similar to our previous optogenetic experiments, hippocampal SD could be reliably induced by a square wave light pulse (5 sec, 488 nm, 15 mW/mm^2, 1p CW laser READYBeam™ Bio2, FISBA AG, SUI) (Fig. 4 B). For practical procedural reasons related to the optrode implant, imaging was carried out in the cortical hemisphere contralateral to hippocampal SD induction (Fig. 4 A). While a widespread coactivation of the imaged CTX (e.g. motor cortex: M2, M1; parietal cortex: Pa) was observed during optogenetically induced hippocampal SD across 12 recordings (4 mice, 3 SD each, one SD stim./d, Fig. 4 B-D), no SD or wave-like invasion resembling SD dynamics were ever observed. In line with this, no activation lags could be found across distant neocortical areas (e.g. M2/P, Fig. 4 E), and CTX continued to show typical transients of Ca^{2+} activity (Fig. 4 B), specifically also with respect to movement (Fig. 4 F, G) (*65*, *66*). Notably, neocortical areas showed an enhanced correlation of activity in the post-stimulation period (Fig. 4 H). Still, similar to our 2p-imaging results in CTX during encephalitis, cortical dynamics across regions also often displayed, although moderately, a reduction of basic fluorescence in the immediate post-stimulation period despite the absence of SD (Fig. 4 B right, 4 C and I, suppl. Fig. 9). Importantly, also during this time, Ca^{2+} transients continued without interruption (Fig. 4 B right). Further, as in our 2p-imaging experiments, the recovery to pre-stimulation basic fluorescence was consistently fast in CTX (<1 min, Fig. 4 J).

In line with our encephalitis and optogenetic experiments before, hippocampal SD prompted increased motion energy during the post-stim. period (Fig. 4 K). Interestingly, while CTX imaging and motion energy signals also showed increased correlation in the post-stim. period (Fig. 4 L), the correlation between hippocampal LFP and motion energy remained unchanged (Fig. 4 M), and the correlation of CTX imaging and hippocampal LFP decreased (Fig. 4 N), indicating divergent post-stim. cortical and hippocampal activity

dynamics. Together, these wide-field imaging experiments of the contralateral hemisphere recapitulated results from our 2p-imaging experiments, and substantiated the evidence that hippocampal SD does not typically propagate to CTX, at least where we imaged. Neocortical Ca^{2+} transients appeared to continue throughout the post-stimulation period without signs of activity depression, and, in contrast to SD dynamics, showed a rapid recovery from reduced basic fluorescence to pre-stimulation conditions. Further, the correlation between CTX activity dynamics and motion energy increased in the post-stimulation period, while it did not between hippocampal LFP and motion energy, and decreased between hippocampal LFP and CTX, suggesting divergent dynamics.

Seizure-associated putative SD in human epilepsy

The current EEG-standard with a bandwidth of 0.5-70 Hz(*67*) renders SD invisible in clinical practice (suppl. Fig. 10). Thus, we finally sought to examine the occurrence, and potentially regional preference of focal electrographic slow shifts at Sz termination in human focal epilepsy through multi-regional Behnke-Fried (BF) electrode recordings, in the context of stereotactic depth macro-electrode recordings (SEEG) during pre-epilepsy-surgery diagnostic work-up (Fig. 5 A, B, Suppl. Fig. 11, Suppl. Table 3, see methods for details). Although not DC-coupled full-bandwidth recordings, these AC recordings included a 0.1 Hz high-pass filter, allowing detection of slow shifts at Sz termination which we labeled putative sSD (psSD).

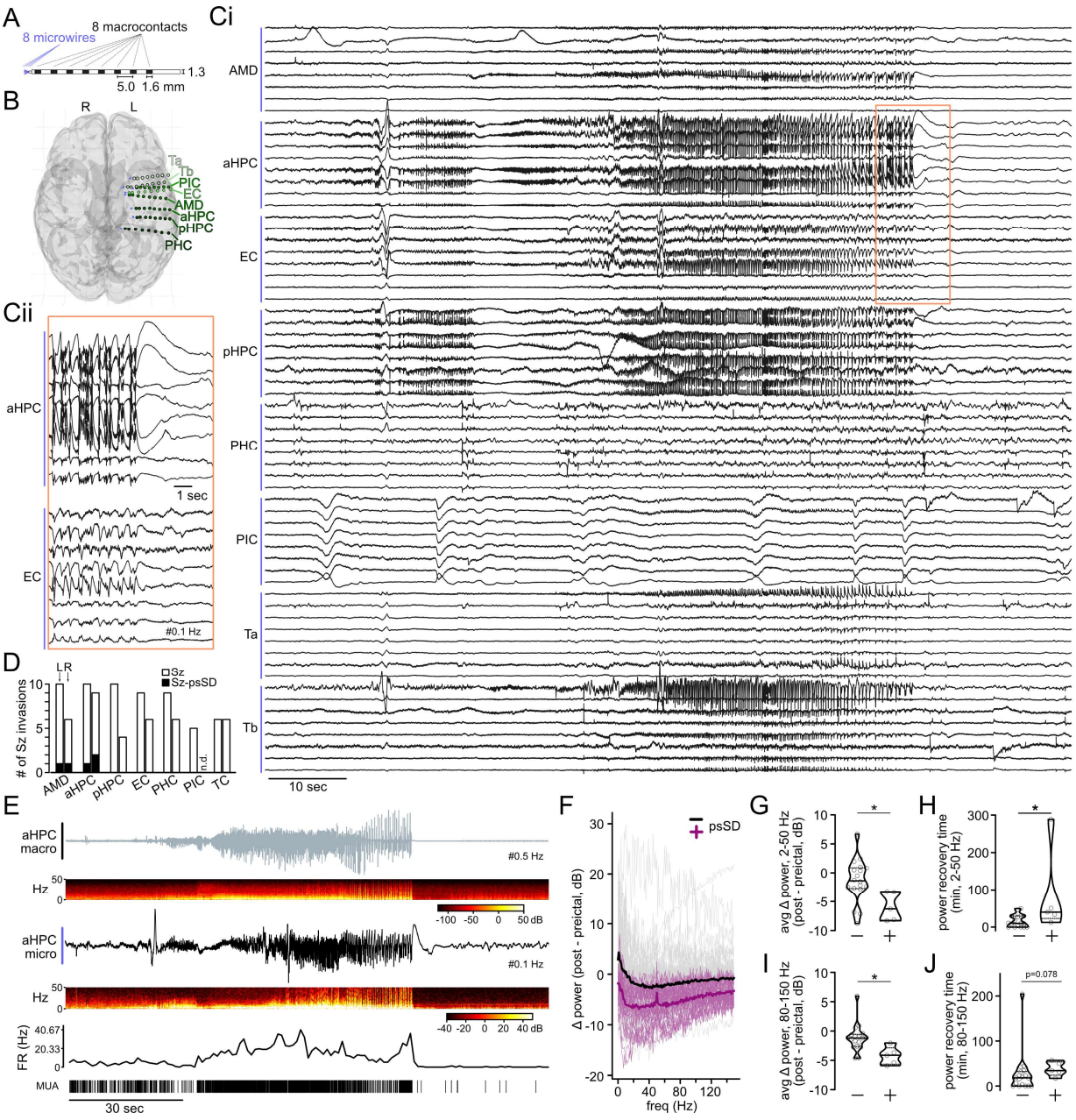

Fig. 5. Putative sSD at Sz termination in BF electrode recordings in human epilepsy

A, Scheme and dimensions of individual Behnke-Fried (BF) electrodes composed of depth-electrode macro-contacts and microwire bundle. **B**, 3D-reconstructed brain MRI and location of implanted BF electrodes. Green dots indicate macro-contact locations, shades of green designate different brain regions and violet markers depict microwire bundles. AMD: amygdala, aHPC: anterior hippocampus, EC: entorhinal cortex, pHPC: posterior hippocampus, PHC: parahippocampal cortex, PIC: piriform cortex, Ta: temporal cortex a, Tb: temporal cortex b. **C i**, LFP traces from BF microwire bundles across recorded regions (0.1 HP filter, referenced to local common average) of a temporomesial focal onset Sz. **C ii**, magnified inset from Ci, aHPC (as marked by orange lines). Note putative sSD (psSD) at Sz termination, confined to HPC. **D**, Regional occurrence count of psSD across all Sz-invaded regions (all Sz/patients included). **E**, aHPC, most distal macro contact trace (top), corresponding microwire trace (middle) and multi-unit activity from the same microwire (bottom). **F**, Change in power between the first postictal minute and the preictal minute. Each line represents one Sz-invaded microwire, color shades indicate Sz-invaded (gray, psSD-neg.) and Sz-psSD-invaded (purple, psSD-pos.) regions, bold lines depict the mean of each group. **G**, Comparison

of respective Δ pre- and post-ictal broadband power (dB, 2-50 Hz) in psSD-neg. (18 events) vs. psSD-pos. (5 events) Sz-invaded regions, unpaired t-test (-1.365 ± 0.8728 [psSD-neg.] vs. -5.870 ± 1.107 [psSD-pos.], p=0.0189). **H**, Comparison of postictal broadband power recovery time (min) of psSD-neg. (18 events) vs. psSD-pos. (5 events) Sz-invaded regions, Mann-Whitney test (16.7 ± 3.84 [sS-neg.] vs. 84.87 ± 51.29 [psSD-pos.], p=0.0112). **I**, Comparison of respective Δ pre- and post-ictal high-gamma power (dB, 80-150 Hz) in psSD-neg. (18 events) vs. psSD-pos. (5 events) Sz-invaded regions, unpaired t-test (-1.184 ± 0.544 [psSD-neg.] vs. -4.227 ± 0.6825 [psSD-pos.], p=0.0117). **J**, Comparison of postictal high-gamma power recovery time (min) of psSD-neg. (18 events) vs. psSD-pos. (5 events) Sz-invaded regions, Mann-Whitney test (27.05 ± 11.00 [psSD-neg.] vs. 37.97 ± 7.08 [psSD-pos.], p=0.078). For entire fig.: All given ± denote s.e.m.. Depiction of violin plots: median (solid lines), quartiles (dotted lines). Depiction of statistical significance: n.s. not significant, *p < 0.05, **p < 0.01.

As an initial cohort, we included four patients (2 female / 2 male patients, age range 23-50 yrs) with refractory focal epilepsy based on different pathologies, a history of post-ictal symptoms comprising PIW, confusion or aphasia, and depth electrodes in the temporal lobe (Fig. 5 B, for implant schemes and clinical information, see suppl. Fig. 11 and suppl. Table 3). Across a total of 272 BF microelectrodes (8/bundle), 7 brain regions (amygdala, hippocampus [ant., post.], entorhinal / parahippocampal / piriform / temporal cortex), and 39 recording days during pre-surgical evaluation, 16 focal-onset seizures were recorded, of which 13 could be analyzed at the microelectrodes (3 excluded for technical reasons). Strikingly, we found what appeared to be localized psSD in the BF microwire recordings (Fig. 5 Ci, Cii) in every patient (4/13 Sz in total). In the per-region analysis of Sz-invasions, in line with our murine recordings, we found psSD to occur primarily in temporomesial regions (hippocampus, amygdala), while it was not detected in the other recorded regions (Fig. 5 C, D). Notably, in 3 of 4 psSD, the invaded region corresponded to the first Sz-invaded region at the macrocontacts, where psSD were not visible (Fig. 5 E top panel, suppl. Table 3). On average, both psSD-neg. and psSD-pos. regions displayed a postictal/post-sSD reduction in spectral power (Fig. 5 F), but psSD-pos. regions showed a more profound decrease, and a delayed recovery to the pre-ictal condition (Fig. 5 G, H). Consistent with our murine results and previous literature(*10*, *14*, *19*, *68*), at the

neuronal unit level, psSD-invasion coincided with a break-down of neuronal firing (Fig. 5 E, middle and bottom panel). To compare neuronal activity independently of stably trackable neuronal units, we used high gamma (80-150 Hz) oscillatory power as a proxy, as previously described(*69*). Again, on average, both psSD-neg. and psSD-pos. regions showed a decreased post-ictal high gamma power, but psSD-pos. regions displayed a stronger reduction, and delayed recovery (Fig. 5 I, J).

In sum, these BF recordings in a cohort of 4 patients showed focal slow shifts at seizure termination suggestive of localized sSD in human focal epilepsy, and point towards an increased propensity of temporomesial regions to experience psSD. Further, in line with the murine experiments, among Sz-invaded areas, psSD-pos. regions took longer to recover to their pre-ictal baseline than psSD-neg. regions.

Discussion

This work suggests that seizure-associated focal spreading depolarization (sSD) is a pathoclinical hallmark of epilepsy, that is, focal sSD triggers distinct clinical symptoms previously attributed to Sz themselves. We find profound region-specific differences in sSD occurrence that hold true across mice and humans, and provide evidence in mice that temporomesial SD causes *post-ictal ambulation* (PIA). PIA is a hallmark feature of post-ictal wandering (PIW), a prominent symptom whose neurobiological underpinnings have remained unclear. Although PIW was famously described by Jean-Marie Charcot already in 1888-1889 in his *Leçons du mardi à Salpêtrière*(*1*), and even though PIW is regularly encountered in clinical epileptology, its precise prevalence has only recently been quantified. Tai and colleagues described a general PIW occurrence rate of 26% in epilepsy patients with focal unaware seizures(*3*). Interestingly, in line with our

experiments, subgroup analyses showed a clear preference of temporal over extratemporal epilepsy (45.0 vs. 10.0 %), and temporal over extratemporal seizures (9.7 vs. 0.8%). In another study, Jin and Inoue found a PIW occurrence rate of 8.3 % in temporal seizures and of 25.2% in TLE patients(*4*). Although not completely congruent, both studies clearly underscore that PIW is a significant entity in epilepsy. Further, PIW is associated with a risk for severe, potentially life-threatening injuries(*1*, *5*), and carries profound socio-economic implications for affected patients (*1*, *5*, *70*). In a still topical case, Charcot described all these aspects in the epilepsy patient *Mr. Me…s* in Paris who would, upon sudden loss of consciousness, come to himself in a different part of the city, or immersed in the river Seine. In the context of such unconscious episodes, *Mr. Men…s*, although always carrying a note by Charcot stating the epilepsy diagnosis and ambulatory automatisms, was considered a thief and jailed by police, and lost his employment at a bronze manufactory (*1*). A recently published case series about PIW in the public in an unclothed state, e.g. following nocturnal seizures, further underscore the social and even legal dimension of the phenomenon(*70*).

While we observed sSD primarily in temporomesial structures, several aspects require discussion in this regard. First, our analyses of mouse and human sSD were based on focal onset seizures with known or suspected onset zones in the temporal lobe (Suppl. Table 3). Therefore, sSD emergence may depend on its spatial relationship to the Sz onset zone (SOZ) and (peri-)lesional tissue. Still, there are basic neuroanatomical features that could inherently predispose e.g. the hippocampus to sSD. First, hippocampal wiring with itself and other regions renders it more excitable than other portions of the brain such as the neocortex(*71*, *72*). In line with this longstanding notion,

603 our hippocampal optogenetic Sz-induction protocol failed to induce seizures in healthy
604 neocortex. At the synaptic level, the CA3 region contains so-called “conditional detonator”
605 synapses that can strongly drive postsynaptic firing(*73*), which may be why CA3 displayed
606 a high propensity for SD upon repetitive mossy fiber stimulation under hyperexcitable
607 conditions in vitro(*74*). Further, aside from its neuronal connectivity, recent data suggests
608 that the hippocampus displays relatively reduced blood oxygenation and neurovascular
609 coupling in comparison to neocortex due to differences in vascular architecture(*75*).
610 Among other potential contributing factors such as subregion-specific oxidative metabolic
611 capacity(*76*), this may make the hippocampus susceptible to an energy shortage during
612 Sz, promoting sSD. We propose that in addition to possible (peri-)lesional vulnerabilities
613 for sSD, basic neuroanatomical differences across brain regions support differential sSD
614 occurrence rates. This carries implications for notions revolving around regional post-ictal
615 EEG signal depression and its spatial overlap with the assumed SOZ(*77*). It is possible
616 that e.g. the hippocampus, even if only secondarily recruited into a Sz, may be at risk for
617 sSD due to its anatomy. This could then prompt post-ictal signal depression in this territory
618 without it being part of the SOZ.
619
620 Adhering to the neuroanatomical argument, regarding the disparate spatiotemporal
621 trajectories of Sz and sSD in our imaging experiments, work by Scharfman on SD
622 susceptibilities of hippocampal sub-regions(*74*) may provide a potential explanation for
623 this unexpected result. We always imaged CA1 contralateral to the TMEV CA1 injection
624 site, and consistently observed a mediolateral Sz spread (CA1 → CA2). sSD mostly
625 travelled the other way, which points towards CA2 or CA3 as the source of sSD(*74*).
626 Based on Scharfman’s dual region electrical recordings, her observation that mossy-fiber-

stimulation-triggered SD in CA3 travelled back to dentate gyrus (DG)(*74*), and our CA1 imaging results, one could hypothesize that CA3-prompted sSD propagate both towards DG and CA1. Alternatively, CA2 could be an sSD source, as it receives strong excitatory input from entorhinal cortex, and has been shown to display enhanced excitability in chronic epilepsy(*78*, *79*). Finally, it is also conceivable that multiple potential sSD generators exist across CA regions.

We can only speculate about the exact nature of sSD1 versus sSD2 in our optical imaging experiments. We believe that sSD1 corresponds to what has been described as *pre-SD excitation*(*19*, *31*, *80*, *81*). This pre-excitation has been observed to typically include a brief increase in neuronal firing and fast LFP oscillations, lasting a few seconds on the initial shoulder of depolarization (see e.g. Herreras et al. [1994] Fig. 1 A, or Nasretdinov et al. [2023] Fig. 4 A)(*19*, *80*). These characteristics fit with our LFP recordings of SD (see e.g. Fig. 3 K left), and intriguingly also, the optical delay between sSD1 and sSD2 (~6 seconds, see results). Further, sSD2 consistently had the highest fluorescence among Sz, sSD1 and sSD2. Thus, optical sSD2 could mark the moment of neuronal depolarization above the inactivation threshold and cessation of firing in SD-invaded regions(*19*, *31*, *80*, *81*). Albeit technically challenging, a combination of in vivo imaging with unit recordings or voltage imaging experiments present viable approaches to support or falsify this speculation.

A main finding of this study is that hippocampal SD triggers PIA, whereas hippocampal Sz-mimics do not. Importantly, this does not *per se* mean that the hippocampus as an anatomical region is the primary driver of the observed phenotype. While a transient

shutdown of hippocampal networks (see Fig. 3 E) will likely contribute to unaware ambulation e.g. through navigational confusion, it is likely that the enhanced locomotion upon hippocampal SD is brought about by a number of interconnected brain regions(*82*, *83*) that interact with the hippocampus and that may be indirectly or directly affected by hippocampal SD, including the septum(*84*, *85*) and mesencephalic structures(*82*, *86*). Clearly also, while in our murine models, sSD was observed only in hippocampus during viral encephalitis, and optogenetic hippocampal SD did not invade imaged neocortical areas, this does not mean that it never does (it can, see (*32*, *33*)), nor that it does not invade other subcortical structures (we hypothesize that it does), nor that it does not invade the hippocampus if emerging elsewhere (e.g. in the neocortex(*32*)).

While much has been learned about SD in neurological research e.g. on migraine or traumatic brain injury(*12–14*), the relationship between SD and clinical symptoms in epilepsy has remained understudied. Part of the reason is that most studies on SD in epilepsy have been carried out in vitro, or under anesthesia (*10*, *11*, *27*, *30*, *51*, *52*), which precludes clinical correlation. At other times, it was not primarily intended to link neurophysiological measures to clinical semiology, i.e. in studies focusing on SD-related Sz termination(*52*, *53*). Of note, different types of epilepsies (e.g. acquired vs. genetic epilepsy) and seizures (focal vs. bilateral tonic clonic) will likely affect the occurrence and spatial extent of SD (e.g. local vs. [bi-]hemispheric), and thus impact clinical phenotypes(*87*). Remarkably, most epilepsy research studies do not specifically distinguish Sz with or without SD, although SD has long been suggested to represent a ‘separate entity’ (see Bureš et al.(*28*), p.10). Based on this suggestion and the results shown here, it may indeed be the case that some of the previously observed

675 neurobiological effects attributed directly to Sz are instead mediated by sSD. Notably, as
676 Sz and sSD can co-occur at the same time in different brain regions, this also extends to
677 clinical semiology. Some previously described “ictal” symptoms may instead present
678 compound semiology based on spatially separate, simultaneous Sz and sSD. Re-visiting
679 reported effects and effect-sizes, and clinical symptoms through the lens of Sz versus
680 sSD will likely propel new diagnostic and therapeutic research on many acute and chronic
681 clinical circumstances that involve seizures, and thus potentially, sSD.
682
683 Due to the current EEG standard (≥0.5 Hz)(*67*), SD is invisible in routine clinical care. As
684 a result, medical professionals regularly encounter post-ictal symptoms, but are blind to
685 SD as a potential major determinant of these phenomena. As there is a traditionally strong
686 focus on the “ictus” in epileptology (underscored by current terminology), such symptoms
687 are then usually related to Sz, and sSD plays little to no role in clinical care. Inversely, it
688 is known in basic research that sSD terminates ongoing Sz(*31*, *52*), but since SD-
689 mediated Sz termination has been studied mostly in vitro or under anesthesia, the clinical
690 impact of sSD could not be studied. Therefore, our results highlight the necessity of a
691 close cross-talk between clinical and basic research disciplines. Clearly, sSD can have
692 potentially life-threatening clinical consequences(*6*, *7*). Thus in our view, caution is
693 required if sSD is proposed as a protective factor of the brain against Sz, and as a
694 potential epilepsy treatment tool(*52*, *54*). However, under specific conditions such as
695 refractory status epilepticus, which involves intensive care settings and general
696 anesthesia, SD may be a treatment option, as its pathoclinical impact is suppressed (by
697 anesthesia). This also applies to electroconvulsive treatment - applied under anesthesia
698 in certain hard-to-treat psychiatric disorders - where new research suggests a potentially

699 beneficial role of SD(*88*). Finally, in other neurological conditions such as stroke, recent
700 basic research points towards a double-edged SD impact. In a rodent model of
701 hippocampal stroke, Boyce and colleagues showed acutely deleterious effects of ipsi-
702 lesional terminal SD, while interestingly, contextual fear conditioning was improved only
703 in mice with contralesional SD 7 days post-stroke(*89*). These examples highlight the
704 necessity of further research into possibly varied roles of SD across the neuropsychiatric
705 disease spectrum. For epileptic seizures, our work supports the notion that sSD
706 constitutes a transient homeostatic break-down of a biological system driven beyond its
707 physiological range of operation(*14*), with acute clinical impact.
708
709 There are of course limitations to this study. First, although our murine findings held true
710 across recording modalities, different murine models of hippocampal Sz and SD, and
711 under healthy (optogenetics) and disease (TMEV) conditions, we do not know whether
712 these findings extend across many different etiologies. Aside from the factors discussed
713 above, the exact parameters that favor sSD emergence in hippocampal Sz are not yet
714 clear, and may include e.g. Sz duration, extent of spatial Sz invasion and hippocampal
715 subfields, Sz dynamics (e.g. tonic vs. clonic), internal state or transition between states
716 (e.g. wakefulness, sleep). Another limitation is that while hippocampal SLE ("Sz-mimics")
717 may approximate naturally occurring hippocampal Sz, the ideal experiment would involve
718 closed-loop sSD inhibition upon hippocampal Sz detection in a chronic epilepsy model.
719 Still, we established this approach for several reasons. First, Sz and sSD trajectories differ
720 profoundly, and the exact point of hippocampal sSD emergence remains unknown,
721 precluding sSD inhibition at its onset. Whether partial sSD blockage during propagation
722 can change clinical symptoms, remains to be determined. Further, it is not known if

723 spatiotemporal precision tools such as optogenetics can block SD on its way. We did not
724 employ pharmacology to reduce sSD duration or amplitude as has been documented
725 before(*90*), as this would change Sz dynamics as well. What's more, the side-effect
726 profiles of some agents that alter SD dynamics, e.g. NMDA-receptor antagonists(*52*),
727 include changes of locomotor behavior, which prevents proper assessment of PIA (*91*).
728 Finally, our optogenetic SLE stimulation allowed for a direct comparison of optogenetic
729 SLE- vs. SD-mediated effects on locomotor activity within the same technical framework.
730 For these reasons, we regard optogenetic SLE stimulation as a suitable tool not just for
731 this study, but a vital option for future research on Sz- vs. SD-mediated effects.
732 Inherently, there are also limitations related to the human data in this study. In our wide-
733 bandwidth AC recordings, the lowest possible high-pass filter was 0.1 Hz for technical
734 reasons, leading to slow shift signal attenuation and morphology alteration. Thus, from
735 the raw signal, we cannot be certain whether the terminal slow shifts indeed corresponded
736 to focal sSD, even if our additional analyses point this way. Further, due to the high-pass
737 filter, it is possible that some terminal slow shifts were missed. Indeed, in two recent
738 studies involving DC-coupled surface or depth electrodes recordings in patients with
739 refractory epilepsy, a higher occurrence rate of slow shifts was reported(*25*, *26*). Notably,
740 while we focused on slow shifts at Sz termination, both Bastanyi et al. and Norby et al.
741 analyzed slow shifts all throughout Sz epochs, in part also during pre- and interictal
742 periods. It remains unclear whether all reported slow shifts solely represented SD, or
743 partly other known slow signal dynamics (e.g. in association with low-voltage fast activity
744 at seizure onset)(*92*, *93*). Another reason for a possible underestimation of the true psSD
745 occurrence rate in our human data is that current depth electrode recordings strongly
746 spatially undersample targeted brain areas. In the near future, this limitation may become

747 softened to some extent, on the heels of recent advances in high-density electrode
748 arrays(*94*–*97*). First steps towards a systematic investigation of sSD in larger patient
749 cohorts will require coordinated efforts by institutions that have access to wide-bandwidth
750 AC or DC-coupled intracranial electrical recordings in epilepsy patients. Ideally, such
751 coordinated efforts will include the establishment of high-fidelity sSD-specific functional
752 biomarkers in human epilepsy. Beyond the currently available recording modalities in
753 clinical practice, one should also consider newly available technology for potential high-
754 fidelity full-bandwidth recordings of Sz, SD and sSD in humans, e.g. biocompatible flexible
755 microtransistors(*32*).
756
757 In sum, this work sets stage for a wider discussion of the pathoclinical role of sSD in
758 epilepsy, and a potential re-consideration of the clinical EEG filter standard(*67*). Beyond
759 post-ictal ambulation, our results suggest that focal sSD could underlie other post-ictal
760 symptoms, e.g. confusion, receptive aphasia, navigational impairment, or defensive-like
761 aggression(*2*, *98*, *99*). Finally, beyond its immediate effects, sSD may play a pathoclinical
762 role in comorbidities of epilepsy, and other diseases encompassing temporal lobe
763 pathology and seizures, e.g. neurodegenerative diseases, which are not primarily treated
764 by epileptologists.
765
766
767
768
769

References:

1. J. M. Charcot, in *Leçons du mardi à la Salpêtrière - Policlinique 1888-1889*, E. Lecrosnier & Babé, Ed. (Bureaux de Progrès médical, Paris, 1889), pp. 302–326.
2. J. C. M. Pottkämper, J. Hofmeijer, J. A. van Waarde, M. J. A. M. van Putten, The postictal state — What do we know? *Epilepsia*. **61**, 1045–1061 (2020).
3. P. Tai, S. Poochikian-Sarkissian, D. Andrade, T. Valiante, M. del Campo, R. Wennberg, Postictal wandering is common after temporal lobe seizures. *Neurology*. **74**, 932–933 (2010).
4. L. Jin, Y. Inoue, Spontaneous periictal leaving behavior: A potential lateralizing sign in mesial temporal lobe epilepsy. *Epilepsia*. **50**, 1560–1565 (2009).
5. A. C. Grant, E. Koziorynska, C. Lushbough, D. Maus, K. Mortati, Acute postictal confusion and violence: Two cases with unfortunate outcomes. *Epilepsy Behav. Case Reports*. **1**, 71–73 (2013).
6. I. Aiba, J. L. Noebels, Spreading depolarization in the brainstem mediates sudden cardiorespiratory arrest in mouse SUDEP models. *Sci. Transl. Med.* **7** (2015), doi:10.1126/scitranslmed.aaa4050.
7. I. C. M. Loonen, N. A. Jansen, S. M. Cain, M. Schenke, R. A. Voskuyl, A. C. Yung, B. Bohnet, P. Kozlowski, R. D. Thijs, M. D. Ferrari, T. P. Snutch, A. M. J. M. Van Den Maagdenberg, E. A. Tolner, Brainstem spreading depolarization and cortical dynamics during fatal seizures in Cacna1a S218L mice. *Brain*. **142**, 412–425 (2019).
8. J. S. Farrell, I. Gaxiola-Valdez, M. D. Wolff, L. S. David, H. I. Dika, B. L. Geeraert, X. R. Wang, S. Singh, S. C. Spanswick, J. F. Dunn, M. C. Antle, P. Federico, G. C. Teskey, Postictal behavioural impairments are due to a severe prolonged hypoperfusion/hypoxia event that is COX-2 dependent. *Elife*. **5**, 1–24 (2016).
9. J. S. Farrell, R. Colangeli, B. Dudok, M. D. Wolff, S. L. Nguyen, J. Jackson, C. T. Dickson, I. Soltesz, G. C. Teskey, In vivo assessment of mechanisms underlying the

795 neurovascular basis of postictal amnesia. *Sci. Rep.* **10**, 1–13 (2020).
796 10. A. A. P. Leao, Spreading Depression of Activity in the Cerebral Cortex. *J. Neurophysiol.*
797 **7**, 359–390 (1944).
798 11. T. Takano, G. F. Tian, W. Peng, N. Lou, D. Lovatt, A. J. Hansen, K. A. Kasischke, M.
799 Nedergaard, Cortical spreading depression causes and coincides with tissue hypoxia.
800 *Nat. Neurosci.* **10**, 754–762 (2007).
801 12. C. L. Lemale, J. Lückl, V. Horst, C. Reiffurth, S. Major, N. Hecht, J. Woitzik, J. P. Dreier,
802 Migraine Aura, Transient Ischemic Attacks, Stroke, and Dying of the Brain Share the
803 Same Key Pathophysiological Process in Neurons Driven by Gibbs–Donnan Forces,
804 Namely Spreading Depolarization. *Front. Cell. Neurosci.* **16**, 1–29 (2022).
805 13. O. Cozzolino, M. Marchese, F. Trovato, E. Pracucci, G. M. Ratto, M. G. Buzzi, F. Sicca,
806 F. M. Santorelli, Understanding spreading depression from headache to sudden
807 unexpected death. *Front. Neurol.* **9**, 1–13 (2018).
808 14. J. P. Dreier, The role of spreading depression, spreading depolarization and spreading
809 ischemia in neurological disease. *Nat. Med.* **17**, 439–447 (2011).
810 15. B. Bosche, R. Graf, R. I. Ernestus, C. Dohmen, T. Reithmeier, G. Brinker, A. J. Strong, J.
811 P. Dreier, J. Woitzik, Recurrent spreading depolarizations after subarachnoid hemorrhage
812 decreases oxygen availability in human cerebral cortex. *Ann. Neurol.* (2010),
813 doi:10.1002/ana.21943.
814 16. J. A. Hartings, N. Andaluz, M. R. Bullock, J. M. Hinzman, B. Mathern, C. Pahl, A. Puccio,
815 L. A. Shutter, A. J. Strong, A. Vagal, J. A. Wilson, J. P. Dreier, L. B. Ngwenya, B.
816 Foreman, L. Pahren, H. Lingsma, D. O. Okonkwo, Prognostic Value of Spreading
817 Depolarizations in Patients with Severe Traumatic Brain Injury. *JAMA Neurol.* **77**, 489–
818 499 (2020).
819 17. J. P. Dreier, S. Major, H. W. Pannek, J. Woitzik, M. Scheel, D. Wiesenthal, P. Martus, M.
820 K. L. Winkler, J. A. Hartings, M. Fabricius, E. J. Speckmann, A. Gorji, Spreading

convulsions, spreading depolarization and epileptogenesis in human cerebral cortex. *Brain*. **135**, 259–275 (2012).

18. C. Dohmen, O. W. Sakowitz, M. Fabricius, B. Bosche, T. Reithmeier, R. I. Ernestus, G. Brinker, J. P. Dreier, J. Woitzik, A. J. Strong, R. Graf, Spreading depolarizations occur in human ischemic stroke with high incidence. *Ann. Neurol.* **63**, 720–728 (2008).

19. A. Nasretdinov, D. Vinokurova, C. L. Lemale, G. Burkhanova-zakirova, K. Chernova, J. Makarova, O. Herreras, J. P. Dreier, R. Khazipov, Diversity of cortical activity changes beyond depression during Spreading Depolarizations. *Nat. Commun.* **14** (2023), doi:10.1038/s41467-023-43509-3.

20. M. Fabricius, S. Fuhr, L. Willumsen, J. P. Dreier, R. Bhatia, M. G. Boutelle, J. A. Hartings, R. Bullock, A. J. Strong, M. Lauritzen, Association of seizures with cortical spreading depression and peri-infarct depolarisations in the acutely injured human brain. *Clin. Neurophysiol.* **119**, 1973–1984 (2008).

21. A. J. Strong, M. Fabricius, M. G. Boutelle, S. J. Hibbins, S. E. Hopwood, R. Jones, M. C. Parkin, M. Lauritzen, Spreading and synchronous depressions of cortical activity in acutely injured human brain. *Stroke*. **33**, 2738–2743 (2002).

22. A. Mayevsky, A. Doron, T. Manor, S. Meilin, N. Zarchin, G. E. Ouaknine, Cortical spreading depression recorded from the human brain using a multiparametric monitoring system. *Brain Res.* **740**, 268–274 (1996).

23. J. P. Dreier, J. Woitzik, M. Fabricius, R. Bhatia, S. Major, C. Drenckhahn, T. N. Lehmann, A. Sarrafzadeh, L. Willumsen, J. A. Hartings, O. W. Sakowitz, J. H. Seemann, A. Thieme, M. Lauritzen, A. J. Strong, Delayed ischaemic neurological deficits after subarachnoid haemorrhage are associated with clusters of spreading depolarizations. *Brain*. **129**, 3224–3237 (2006).

24. C. Drenckhahn, M. K. L. Winkler, S. Major, M. Scheel, E. J. Kang, A. Pinczolits, C. Grozea, J. A. Hartings, J. Woitzik, J. P. Dreier, Correlates of spreading depolarization in

847 human scalp electroencephalography. *Brain*. **135**, 853–868 (2012).
848 25. Z. J. R. Bastany, S. Askari, G. A. Dumont, C. Kellinghaus, A. Kazemi, A. Gorji,
849 Association of cortical spreading depression and seizures in patients with medically
850 intractable epilepsy. *Clin. Neurophysiol.* **131**, 2861–2874 (2020).
851 26. J. H. Norby, D. Hummel, N. Ricks, J. Rolston, S. Rahimpour, R. Cowan, J. Voipio, A. J.
852 Trevelyan, E. H. Smith, R. R. Parrish, Rodent and human seizures demonstrate a
853 dynamic interplay with spreading depolarizations. *Neurobiol. Dis.* **211** (2025),
854 doi:10.1016/j.nbd.2025.106937.
855 27. M. Sramka, G. Brozek, J. Bures, P. Nadvornik, Functional Ablation by Spreading
856 Depression: Possible Use in Human Stereotactic Neurosurgery. *Appl. Neurophysiol.* **40**,
857 48–61 (1978).
858 28. J. Bureš, O. Burešová, J. Křivánek, *The mechanism and applications of Leao's spreading*
859 *depression of electroencephalographic activity* (1974).
860 29. P. E. Kunkler, R. P. Kraig, Hippocampal spreading depression bilaterally activates the
861 caudal trigeminal nucleus in rodents. *Hippocampus*. **13**, 835–844 (2003).
862 30. B. E. Lindquist, C. W. Shuttleworth, Adenosine receptor activation is responsible for
863 prolonged depression of synaptic transmission after spreading depolarization in brain
864 slices. *Neuroscience*. **223**, 365–376 (2012).
865 31. A. Bragin, M. Penttonen, G. Buzsáki, Termination of epileptic afterdischarge in the
866 hippocampus. *J. Neurosci.* **17**, 2567–2579 (1997).
867 32. A. Bonaccini Calia, E. Masvidal-Codina, T. M. Smith, N. Schäfer, D. Rathore, E.
868 Rodríguez-Lucas, X. Illa, J. M. De la Cruz, E. Del Corro, E. Prats-Alfonso, D. Viana, J.
869 Bousquet, C. Hébert, J. Martínez-Aguilar, J. R. Sperling, M. Drummond, A. Halder, A.
870 Dodd, K. Barr, S. Savage, J. Fornell, J. Sort, C. Guger, R. Villa, K. Kostarelos, R. C.
871 Wykes, A. Guimerà-Brunet, J. A. Garrido, Full-bandwidth electrophysiology of seizures
872 and epileptiform activity enabled by flexible graphene microtransistor depth neural

probes. *Nat. Nanotechnol.* (2021), doi:10.1038/s41565-021-01041-9.

33. F. Bahari, P. Ssentongo, J. Liu, J. Kimbugwe, C. Curay, S. J. Schiff, B. J. Gluckman, Seizure-associated spreading depression is a major feature of ictal events in two animal models of chronic epilepsy. *bioRxiv*, 455519 (2020).

34. J. Aquino-Cias, S. Belceva, J. Bureš, E. Fifková, The influence of thalamic spreading depression on cortical and reticular unit activity in the rat. *Brain Res.* **1**, 77–85 (1966).

35. E. Fifková, Leao's Spreading Depression in the Thalamic Nuclei of Rat. *Experientia*. **20**, 635–637 (1964).

36. D. R. Kramer, T. Fujii, I. Ohiorhenuan, C. Y. Liu, Cortical spreading depolarization: Pathophysiology, implications, and future directions. *J. Clin. Neurosci.* **24**, 22–27 (2016).

37. L. Kros, K. Lykke-Hartmann, K. Khodakhah, Increased susceptibility to cortical spreading depression and epileptiform activity in a mouse model for FHM2. *Sci. Rep.* **8**, 1–12 (2018).

38. C. Reiffurth, M. Alam, M. Zahedi-Khorasani, S. Major, J. P. Dreier, Na+/K+-ATPase α isoform deficiency results in distinct spreading depolarization phenotypes. *J. Cereb. Blood Flow Metab.* **40**, 622–638 (2020).

39. M. M. Haglund, P. A. Schwartzkroin, Role of Na-K pump potassium regulation and IPSPs in seizures and spreading depression in immature rabbit hippocampal slices. *J. Neurophysiol.* **63**, 225–239 (1990).

40. C. Nicholson, J. M. Phillips, C. Tobias, R. P. Kraig, in *Ion-Selective Microelectrodes and Their Use in Excitable Tissues* (1981).

41. R. P. Kraig, C. R. Ferreira Filho, C. Nicholson, Alkaline and acid transients in cerebellar microenvironment. *J. Neurophysiol.* (1983), doi:10.1152/jn.1983.49.3.831.

42. A. Gorji, D. Scheller, H. Straub, F. Tegtmeier, R. Köhling, J. M. Höhling, I. Tuxhorn, A. Ebner, P. Wolf, H. W. Panneck, F. Oppel, E. J. Speckmann, Spreading depression in human neocortical slices. *Brain Res.* **906**, 74–83 (2001).

43. D. Y. Chung, H. Sadeghian, T. Qin, S. Lule, H. Lee, F. Karakaya, S. Goins, F. Oka, M. A. Yaseen, T. Houben, E. A. Tolner, A. M. J. M. Van Den Maagdenberg, M. J. Whalen, S. Sakadžić, C. Ayata, Determinants of optogenetic cortical spreading depolarizations. *Cereb. Cortex*. **29**, 1150–1161 (2019).

44. T. Houben, I. C. M. Loonen, S. M. Baca, M. Schenke, J. H. Meijer, M. D. Ferrari, G. M. Terwindt, R. A. Voskuyl, A. Charles, A. M. J. M. Van Den Maagdenberg, E. A. Tolner, Optogenetic induction of cortical spreading depression in anesthetized and freely behaving mice. *J. Cereb. Blood Flow Metab.* **37**, 1641–1655 (2017).

45. E. Masvidal-Codina, T. M. Smith, D. Rathore, Y. Gao, X. Illa, E. Prats-Alfonso, E. Del Corro, A. B. Calia, G. Rius, I. Martin-Fernandez, C. Guger, P. Reitner, R. Villa, J. A. Garrido, A. Guimera-Brunet, R. C. Wykes, Characterization of optogenetically-induced cortical spreading depression in awake mice using graphene micro-transistor arrays. *J. Neural Eng.* **18** (2021), doi:10.1088/1741-2552/abecf3.

46. K. Sugimoto, D. Y. Chung, M. Böhm, P. Fischer, T. Takizawa, S. Aslihan Aykan, T. Qin, T. Yanagisawa, A. Harriott, F. Oka, M. A. Yaseen, S. Sakadžić, C. Ayata, Peri-Infarct Hot-Zones Have Higher Susceptibility to Optogenetic Functional Activation-Induced Spreading Depolarizations. *Stroke*. **51**, 2526–2535 (2020).

47. M. Dell'Orco, J. E. Weisend, N. I. Perrone-Bizzozero, A. P. Carlson, R. A. Morton, D. N. Linsenbardt, C. W. Shuttleworth, Repetitive spreading depolarization induces gene expression changes related to synaptic plasticity and neuroprotective pathways. *Front. Cell. Neurosci.* **17** (2023), doi:10.3389/fncel.2023.1292661.

48. O. Chever, S. Zerimech, P. Scalmani, L. Lemaire, L. Pizzamiglio, A. Loucif, M. Ayrault, M. Krupa, M. Desroches, F. Duprat, I. Léna, S. Cestèle, M. Mantegazza, Initiation of migraine-related cortical spreading depolarization by hyperactivity of GABAergic neurons and NaV1.1 channels. *J. Clin. Invest.* **131**, 1–15 (2021).

49. N. Zhou, G. R. J. Gordon, D. Feighan, B. A. MacVicar, Transient swelling, acidification,

and mitochondrial depolarization occurs in neurons but not astrocytes during spreading depression. *Cereb. Cortex*. **20**, 2614–2624 (2010).

50. C. W. Shuttleworth, R. D. Andrew, Y. Akbari, C. Ayata, R. Balu, K. C. Brennan, M. Boutelle, A. P. Carlson, J. P. Dreier, M. Fabricius, E. Farkas, B. Foreman, R. Helbok, N. Henninger, S. L. Jewell, S. C. Jones, S. A. Kirov, B. E. Lindquist, C. B. Maciel, D. Okonkwo, K. M. Reinhart, R. M. Robertson, E. S. Rosenthal, T. Watanabe, J. A. Hartings, Which Spreading Depolarizations Are Deleterious To Brain Tissue? *Neurocrit. Care*. **32**, 317–322 (2020).

51. A. Gorji, E. J. Speckmann, Spreading depression enhances the spontaneous epileptiform activity in human neocortical tissues. *Eur. J. Neurosci.* (2004), doi:10.1111/j.0953-816X.2004.03436.x.

52. I. Tamim, D. Y. Chung, A. L. de Morais, I. C. M. Loonen, T. Qin, A. Misra, F. Schlunk, M. Endres, S. J. Schiff, C. Ayata, Spreading depression as an innate antiseizure mechanism. *Nat. Commun.* **12**, 1–15 (2021).

53. K. Heuser, C. G. Nome, K. H. Pettersen, K. S. Åbjørsbråten, V. Jensen, W. Tang, R. Sprengel, E. Taubøll, E. A. Nagelhus, R. Enger, Ca 2+ Signals in Astrocytes Facilitate Spread of Epileptiform Activity. *Cereb. Cortex*. **28**, 4036–4048 (2018).

54. R. Enger, K. Heuser, Astrocytes as critical players of the fine balance between inhibition and excitation in the brain: spreading depolarization as a mechanism to curb epileptic activity. *Front. Netw. Physiol.* **4**, 1–8 (2024).

55. J. E. Libbey, N. J. Kirkman, M. C. P. Smith, T. Tanaka, K. S. Wilcox, H. S. White, R. S. Fujinami, Seizures following picornavirus infection. *Epilepsia*. **49**, 1066–1074 (2008).

56. L. J. Hirsch, M. W. K. Fong, M. Leitinger, S. M. LaRoche, S. Beniczky, N. S. Abend, J. W. Lee, C. J. Wusthoff, C. D. Hahn, M. B. Westover, E. E. Gerard, S. T. Herman, H. A. Haider, G. Osman, A. Rodriguez-Ruiz, C. B. Maciel, E. J. Gilmore, A. Fernandez, E. S. Rosenthal, J. Claassen, A. M. Husain, J. Y. Yoo, E. L. So, P. W. Kaplan, M. R. Nuwer, M.

van Putten, R. Sutter, F. W. Drislane, E. Trinka, N. Gaspard, American Clinical Neurophysiology Society's Standardized Critical Care EEG Terminology: 2021 Version. *J. Clin. Neurophysiol.* **38**, 1–29 (2021).

57. R. Enger, W. Tang, G. F. Vindedal, V. Jensen, P. J. Helm, R. Sprengel, L. L. Looger, E. A. Nagelhus, Dynamics of ionic shifts in cortical spreading depression. *Cereb. Cortex*. **25**, 4469–4476 (2015).

58. M. Wenzel, J. P. Hamm, D. S. Peterka, R. Yuste, Reliable and Elastic Propagation of Cortical Seizures In Vivo. *Cell Rep.* **19**, 2681–2693 (2017).

59. M. Wenzel, J. P. Hamm, D. S. Peterka, R. Yuste, Acute Focal Seizures Start As Local Synchronizations of Neuronal Ensembles. *J. Neurosci.* **39**, 8562–8575 (2019).

60. W. Truccolo, J. A. Donoghue, L. R. Hochberg, E. N. Eskandar, J. R. Madsen, W. S. Anderson, E. N. Brown, E. Halgren, S. S. Cash, Single-neuron dynamics in human focal epilepsy. *Nat Neurosci*. **14**, 635–641 (2011).

61. E. J. Henriksen, L. L. Colgin, C. A. Barnes, M. P. Witter, M. B. Moser, E. I. Moser, Spatial representation along the proximodistal axis of CA1. *Neuron*. **68**, 127–137 (2010).

62. M. dal Maschio, J. C. Donovan, T. O. Helmbrecht, H. Baier, Linking Neurons to Network Function and Behavior by Two-Photon Holographic Optogenetics and Volumetric Imaging. *Neuron*. **94**, 774-789.e5 (2017).

63. B. K. Andrasfalvy, B. V. Zemelman, J. Tang, A. Vaziri, Two-photon single-cell optogenetic control of neuronal activity by sculpted light. *Proc. Natl. Acad. Sci. U. S. A.* **107**, 11981–11986 (2010).

64. J. Couto, S. Musall, X. R. Sun, A. Khanal, S. Gluf, S. Saxena, I. Kinsella, T. Abe, J. P. Cunningham, L. Paninski, A. K. Churchland, Chronic, cortex-wide imaging of specific cell populations during behavior. *Nat. Protoc.* **16**, 3241–3263 (2021).

65. S. Musall, M. T. Kaufman, A. L. Juavinett, S. Gluf, A. K. Churchland, Single-trial neural dynamics are dominated by richly varied movements. *Nat. Neurosci.* **22**, 1677–1686

(2019).

66. I. Orsolic, M. Rio, T. D. Mrsic-Flogel, P. Znamenskiy, Mesoscale cortical dynamics reflect the interaction of sensory evidence and temporal expectation during perceptual decision-making. *Neuron*. **109**, 1861-1875.e10 (2021).

67. M. E. Peltola, M. Leitinger, J. J. Halford, K. P. Vinayan, K. Kobayashi, R. M. Pressler, I. Mindruta, L. C. Mayor, L. Lauronen, S. Beniczky, Routine and sleep EEG: Minimum recording standards of the International Federation of Clinical Neurophysiology and the International League Against Epilepsy. *Clin. Neurophysiol.* **147**, 108–120 (2023).

68. H. Kager, W. J. Wadman, G. G. Somjen, Conditions for the triggering of spreading depression studied with computer simulations. *J. Neurophysiol.* **88**, 2700–2712 (2002).

69. S. A. Weiss, G. P. Banks, G. M. McKhann, R. R. Goodman, R. G. Emerson, A. J. Trevelyan, C. A. Schevon, Ictal high frequency oscillations distinguish two types of seizure territories in humans. *Brain*. **136**, 3796–3808 (2013).

70. H. S. Wortzel, L. A. Strom, A. C. Anderson, E. H. Maa, M. Spitz, Disrobing Associated with Epileptic Seizures and Forensic Implications. *J. Forensic Sci.* **57**, 550–552 (2012).

71. R. Jung, Hirnelektrische Untersuchungen über den Elektrokrampf: Die Erregungsabläufe in corticalen und subcorticalen Hirnregionen bei Katze und Hund. *Arch. F. Psychiatr. U. Z. Neur.* **183**, 206–244 (1949).

72. P. Andersen, R. Morris, D. Amaral, T. Bliss, J. O'Keefe, *The Hippocampus Book* (Oxford University Press, 2006; https://doi.org/10.1093/acprof:oso/9780195100273.001.0001).

73. D. A. Henze, L. Wittner, G. Buzsáki, Single granule cells reliably discharge targets in the hippocampal CA3 network in vivo. *Nat. Neurosci.* **5**, 790–795 (2002).

74. H. E. Scharfman, Hyperexcitability in combined entorhinal/hippocampal slices of adult rat after exposure to brain-derived neurotrophic factor. *J. Neurophysiol.* **78**, 1082–1095 (1997).

75. K. Shaw, L. Bell, K. Boyd, D. M. Grijseels, D. Clarke, O. Bonnar, H. S. Crombag, C. N.

Hall, Neurovascular coupling and oxygenation are decreased in hippocampus compared to neocortex because of microvascular differences. *Nat. Commun.* **12**, 1–16 (2021).

76. C. Davolio, J. T. Greenamyre, Selective vulnerability of the CA1 region of hippocampus to the indirect excitotoxic effects of malonic acid. *Neurosci. Lett.* **192**, 29–32 (1995).

77. R. Di Giacomo, R. Uribe-San-Martin, R. Mai, S. Francione, L. Nobili, I. Sartori, F. Gozzo, V. Pelliccia, M. Onofrj, G. Lo Russo, M. de Curtis, L. Tassi, Stereo-EEG ictal/interictal patterns and underlying pathologies. *Seizure*. **72**, 54–60 (2019).

78. V. Chevaleyre, S. A. Siegelbaum, Strong CA2 pyramidal neuron synapses define a powerful disynaptic cortico-hippocampal loop. *Neuron*. **66**, 560–572 (2010).

79. A. C. Whitebirch, J. J. LaFrancois, S. Jain, P. Leary, B. Santoro, S. A. Siegelbaum, H. E. Scharfman, Enhanced excitability of the hippocampal CA2 region and its contribution to seizure activity in a mouse model of temporal lobe epilepsy. *Neuron*. **110**, 3121-3138.e8 (2022).

80. O. Herreras, C. Largo, J. M. Ibarz, G. G. Somjen, R. M. Del Río, Role of neuronal synchronizing mechanisms in the propagation of spreading depression in the in vivo hippocampus. *J. Neurosci.* **14**, 7087–7098 (1994).

81. V. Dzhala, I. Khalilov, Y. Ben-Ari, R. Khazipov, Neuronal mechanisms of the anoxia-induced network oscillations in the rat hippocampus in vitro. *J. Physiol.* **536**, 521–531 (2001).

82. A. J. Pernía-Andrade, N. Wenger, M. S. Esposito, P. Tovote, Circuits for State-Dependent Modulation of Locomotion. *Front. Hum. Neurosci.* **15**, 1–20 (2021).

83. S. Arber, R. M. Costa, Networking brainstem and basal ganglia circuits for movement. *Nat. Rev. Neurosci.* **23**, 342–360 (2022).

84. F. Fuhrmann, D. Justus, L. Sosulina, H. Kaneko, T. Beutel, D. Friedrichs, S. Schoch, M. K. Schwarz, M. Fuhrmann, S. Remy, Locomotion, Theta Oscillations, and the Speed-Correlated Firing of Hippocampal Neurons Are Controlled by a Medial Septal

Glutamatergic Circuit. *Neuron*. **86**, 1253–1264 (2015).

85. H. S. Wirtshafter, M. A. Wilson, Locomotor and Hippocampal Processing Converge in the Lateral Septum. *Curr. Biol.* **29**, 3177-3192.e3 (2019).

86. P. Mocellin, O. Barnstedt, K. Luxem, H. Kaneko, S. Vieweg, J. U. Henschke, D. Dalügge, F. Fuhrmann, A. Karpova, J. M. P. Pakan, M. R. Kreutz, S. Mikulovic, S. Remy, A septal-ventral tegmental area circuit drives exploratory behavior. *Neuron*. **112**, 1020-1032.e7 (2024).

87. I. Aiba, Y. Ning, J. L. Noebels, A hyperthermic seizure unleashes a surge of spreading depolarizations in Scn1a-deficient mice. *JCI Insight*. **8** (2023), doi:10.1172/jci.insight.170399.

88. Z. P. Rosenthal, J. B. Majeski, A. Somarowthu, D. K. Quinn, B. E. Lindquist, M. E. Putt, A. Karaj, C. G. Favilla, W. B. Baker, G. Hosseini, J. P. Rodriguez, M. A. Cristancho, Y. I. Sheline, C. W. Shuttleworth, C. C. Abbott, A. G. Yodh, E. M. Goldberg, Electroconvulsive therapy generates a postictal wave of spreading depolarization in mice and humans. *Nat. Commun.* **16** (2025), doi:10.1038/s41467-025-59900-1.

89. A. K. J. Boyce, Y. Fouad, R. C. Gom, D. M. Ashby, C. Martins-Silva, L. Molina, T. Füzesi, C. Ens, W. Nicola, A. McGirr, G. C. Teskey, R. J. Thompson, Contralesional hippocampal spreading depolarization promotes functional recovery after stroke. *Nat. Commun.* . **16**, 1–20 (2025).

90. A. Klass, R. Sánchez-Porras, E. Santos, Systematic review of the pharmacological agents that have been tested against spreading depolarizations. *J. Cereb. Blood Flow Metab.* **38**, 1149–1179 (2018).

91. W. Danysz, U. Essmann, I. Bresink, R. Wilk, Glutamate antagonists have different effects on spontaneous locomotor activity in rats. *Pharmacol. Biochem. Behav.* **48**, 111–118 (1994).

92. A. Ikeda, K. Terada, N. Mikuni, R. C. Burgess, Y. Comair, W. Taki, T. Hamano, J. Kimura,

H. O. Lüders, H. Shibasaki, Subdural recording of ictal DC shifts in neocortical seizures in humans. *Epilepsia*. **37**, 662–674 (1996).

93. V. Gnatkovsky, M. De Curtis, C. Pastori, F. Cardinale, G. Lo Russo, R. Mai, L. Nobili, I. Sartori, L. Tassi, S. Francione, Biomarkers of epileptogenic zone defined by quantified stereo-EEG analysis. *Epilepsia*. **55**, 296–305 (2014).

94. J. E. Chung, K. K. Sellers, M. K. Leonard, L. Gwilliams, D. Xu, M. E. Dougherty, V. Kharazia, S. L. Metzger, M. Welkenhuysen, B. Dutta, E. F. Chang, High-density single-unit human cortical recordings using the Neuropixels probe. *Neuron*. **110**, 2409-2421.e3 (2022).

95. A. C. Paulk, Y. Kfir, A. R. Khanna, M. L. Mustroph, E. M. Trautmann, D. J. Soper, S. D. Stavisky, M. Welkenhuysen, B. Dutta, K. V. Shenoy, L. R. Hochberg, R. M. Richardson, Z. M. Williams, S. S. Cash, *Large-scale neural recordings with single neuron resolution using Neuropixels probes in human cortex* (Springer US, 2022), vol. 25.

96. K. K. Sellers, J. E. Chung, J. Zhou, M. G. Triplett, H. E. Dawes, R. Haque, E. F. Chang, Thin-film microfabrication and intraoperative testing of μeCoG and iEEG depth arrays for sense and stimulation. *J. Neural Eng.* **18** (2021), doi:10.1088/1741-2552/ac1984.

97. K. Lee, A. C. Paulk, Y. G. Ro, D. R. Cleary, K. J. Tonsfeldt, Y. Kfir, J. S. Pezaris, Y. Tchoe, J. Lee, A. M. Bourhis, R. Vatsyayan, J. R. Martin, S. M. Russman, J. C. Yang, A. Baohan, R. M. Richardson, Z. M. Williams, S. I. Fried, U. Hoi Sang, A. M. Raslan, S. Ben-Haim, E. Halgren, S. S. Cash, S. A. Dayeh, Flexible, scalable, high channel count stereo-electrode for recording in the human brain. *Nat. Commun.* **15** (2024), doi:10.1038/s41467-023-43727-9.

98. W. H. Theodore, R. J. Porter, J. K. Penry, Complex partial seizures: Clinical characteristics and differential diagnosis. *Neurology*. **33**, 1115–21 (1983).

99. G. Bronsard, F. Bartolomei, Rhythms, rhythmicity and aggression. *J. Physiol. Paris*. **107**, 327–334 (2013).

100. H. Dana, T. W. Chen, A. Hu, B. C. Shields, C. Guo, L. L. Looger, D. S. Kim, K. Svoboda, Thy1-GCaMP6 transgenic mice for neuronal population imaging in vivo. *PLoS One*. **9**, e108697 (2014).

101. N. Masala, M. Mittag, E. A. Giovannetti, D. A. O'Neil, F. Distler, P. Rupprecht, F. Helmchen, R. Yuste, M. Fuhrmann, H. Beck, M. Wenzel, T. Kelly, Aberrant hippocampal Ca2+ micro-waves following synapsin-dependent adeno-associated viral expression of Ca2+ indicators. *Elife* (2024), doi:https://doi.org/10.7554/eLife.93804.1.

102. J. B. Wekselblatt, E. D. Flister, D. M. Piscopo, C. M. Niell, Large-scale imaging of cortical dynamics during sensory perception and behavior. *J. Neurophysiol.* **115**, 2852–2866 (2016).

103. J. E. Libbey, N. J. Kennett, K. S. Wilcox, H. S. White, R. S. Fujinami, Lack of Correlation of Central Nervous System Inflammation and Neuropathology with the Development of Seizures following Acute Virus Infection. *J. Virol.* **85**, 8149–8157 (2011).

104. S. Bröer, C. Käufer, V. Haist, L. Li, I. Gerhauser, M. Anjum, M. Bankstahl, W. Baumgärtner, W. Löscher, Brain inflammation, neurodegeneration and seizure development following picornavirus infection markedly differ among virus and mouse strains and substrains. *Exp. Neurol.* **279**, 57–74 (2016).

105. K. A. Stewart, K. S. Wilcox, R. S. Fujinami, H. S. White, Development of postinfection epilepsy after Theiler's virus infection of C57BL/6 mice. *J Neuropathol Exp Neurol*. **69**, 1210–1219 (2010).

106. A. B. DePaula-Silva, T. J. Hanak, J. E. Libbey, R. S. Fujinami, Theiler's murine encephalomyelitis virus infection of SJL/J and C57BL/6J mice: Models for multiple sclerosis and epilepsy. *J Neuroimmunol*. **308**, 30–42 (2017).

107. E. S. Boyden, F. Zhang, E. Bamberg, G. Nagel, K. Deisseroth, Millisecond-timescale, genetically targeted optical control of neural activity. *Nat Neurosci*. **8**, 1263–1268 (2005).

108. N. Masala, M. Pofahl, A. N. Haubrich, K. U. Sameen Islam, N. Nikbakht, M. Pasdarnavab,

1107 K. Bohmbach, K. Araki, F. Kamali, C. Henneberger, K. Golcuk, L. A. Ewell, S. Blaess, T.
1108 Kelly, H. Beck, Targeting aberrant dendritic integration to treat cognitive comorbidities of
1109 epilepsy. *Brain* (2022), doi:10.1093/brain/awac455.
1110 109. M. Pofahl, N. Nikbakht, A. N. Haubrich, T. Nguyen, N. Masala, F. Distler, O. Braganza, J.
1111 H. Macke, L. A. Ewell, K. Golcuk, H. Beck, Synchronous activity patterns in the dentate
1112 gyrus during immobility. *Elife*. **10**, 1–29 (2021).
1113 110. N. Nikbakht, M. Pofahl, A. Miguel-López, F. Kamali, T. Tchumatchenko, H. Beck, Efficient
1114 encoding of aversive location by CA3 long-range projections. *Cell Rep.* **43** (2024),
1115 doi:10.1016/j.celrep.2024.113957.
1116 111. M. Wenzel, S. Han, E. H. Smith, E. Hoel, B. Greger, P. A. House, R. Yuste, Reduced
1117 Repertoire of Cortical Microstates and Neuronal Ensembles in Medically Induced Loss of
1118 Consciousness. *Cell Syst.* **8**, 467–474 (2019).
1119 112. M. Wenzel, A. Leunig, S. Han, D. S. Peterka, R. Yuste, Prolonged anesthesia alters brain
1120 synaptic architecture. *Proc. Natl. Acad. Sci.* **118**, e2023676118 (2021).
1121 113. J. Pitsch, K. M. J. van Loo, M. Gallus, A. Dik, D. Kamalizade, A. K. Baumgart, V.
1122 Gnatkovsky, J. A. Müller, T. Opitz, G. Hicking, V. N. Naik, L. Wachsmuth, C. Faber, R.
1123 Surges, C. Kurts, S. Schoch, N. Melzer, A. J. Becker, CD8+ T-Lymphocyte–Driven Limbic
1124 Encephalitis Results in Temporal Lobe Epilepsy. *Ann. Neurol.* (2020),
1125 doi:10.1002/ana.26000.
1126 114. J. Pitsch, J. C. Kuehn, V. Gnatkovsky, J. A. Müller, K. M. J. van Loo, M. de Curtis, H.
1127 Vatter, S. Schoch, C. E. Elger, A. J. Becker, Anti-epileptogenic and Anti-convulsive
1128 Effects of Fingolimod in Experimental Temporal Lobe Epilepsy. *Mol. Neurobiol.* **56**, 1825–
1129 1840 (2019).
1130 115. M. S. Kehl, S. Mackay, K. Ohla, M. Schneider, V. Borger, R. Surges, M. Spehr, F.
1131 Mormann, Single-neuron representations of odours in the human brain. *Nature*. **634**,
1132 626–634 (2024).

116. U. Topalovic, S. Barclay, C. Ling, A. Alzuhair, W. Yu, V. Hokhikyan, H. Chandrakumar, D. Rozgic, W. Jiang, S. Basir-Kazeruni, S. L. Maoz, C. S. Inman, M. Stangl, J. Gill, A. Bari, A. Fallah, D. Eliashiv, N. Pouratian, I. Fried, N. Suthana, D. Markovic, A wearable platform for closed-loop stimulation and recording of single-neuron and local field potential activity in freely moving humans. *Nat. Neurosci.* **26**, 517–527 (2023).

117. A. Misra, J. F. Burke, A. G. Ramayya, J. Jacobs, M. R. Sperling, K. A. Moxon, M. J. Kahana, J. J. Evans, A. D. Sharan, Methods for implantation of micro-wire bundles and optimization of single/multi-unit recordings from human mesial temporal lobe. *J. Neural Eng.* **11** (2014), doi:10.1088/1741-2560/11/2/026013.

118. J. C. Williams, R. L. Rennaker, D. R. Kipke, Long-term neural recording characteristics of wire microelectrode arrays implanted in cerebral cortex. *Brain Res. Protoc.* **4**, 303–313 (1999).

119. S. Smeijers, W. Coudyzer, E. Keirse, V. Bougou, T. Decramer, T. Theys, Direct visualization of microwires in hybrid depth electrodes using high-resolution photon-counting CT. *Epilepsia Open*. **9**, 2518–2521 (2024).

120. Z. Fu, U. Rutishauser, in *Encyclopedia of the Human Brain* (Elsevier, 2025), pp. 42–58.

121. A. A. Carlson, U. Rutishauser, A. N. Mamelak, Safety and utility of hybrid depth electrodes for seizure localization and single-unit neuronal recording. *Stereotact. Funct. Neurosurg.* **96**, 311–319 (2018).

122. J. Niediek, J. Boström, C. E. Elger, F. Mormann, Reliable analysis of single-unit recordings from the human brain under noisy conditions: Tracking neurons over hours. *PLoS One*. **11**, e0166598 (2016).

123. S. Musall, X. R. Sun, H. Mohan, X. An, S. Gluf, S. J. Li, R. Drewes, E. Cravo, I. Lenzi, C. Yin, B. M. Kampa, A. K. Churchland, Pyramidal cell types drive functionally distinct cortical activity patterns during decision-making. *Nat. Neurosci.* **26**, 495–505 (2023).

124. W. E. Allen, I. V. Kauvar, M. Z. Chen, E. B. Richman, S. J. Yang, K. Chan, V. Gradinaru,

B. E. Deverman, L. Luo, K. Deisseroth, Global Representations of Goal-Directed Behavior in Distinct Cell Types of Mouse Neocortex. *Neuron*. **94**, 891-907.e6 (2017).

Acknowledgements: We sincerely thank Lea Adenauer and Nele Neumann for outstanding technical support, and Negar Nikbakth, Nicola Masala, and Martin Pofahl for technical advice. We appreciate Lisa Rottenfußer's support and input during her M.Sc. lab rotation. In general, we are grateful to members of the Wenzel, Beck, Ewell, and Mormann laboratories for comments. This work was supported by the BONFOR Program at University of Bonn (M.W.: #2019-2-04), the Hertie Network of Excellence in Clinical Neuroscience (M.W.: #P1200008), and the German Research Foundation (DFG; SFB1089 to M.W., L.E., H.B., and #504342801 to M.W.). The work was further supported by the iBehave network (M.W., S.M., H.B.), the Helmholtz association (S.M.: VH-NG-1611), and the European Research Council (M.W.: StG #101039945). We also acknowledge the support of the Viral Vector Service Core Facility, and the Imaging Core Facility of the Bonn Technology Campus Life Sciences funded by the Deutsche Forschungsgemeinschaft (DFG, German Research Foundation, project #388169927).

Author contributions: M.W. conceived the project. M.W. and B.M. wrote the paper with input from all authors. Experimental contributions: Multimodal 2-photon imaging experiments: B.M., M.W., M.K., M.B., T.T., T.O.. Multimodal 1-photon imaging experiments: N.B., S.M.. Tetrode recordings: A.N.H., M.K.. Wireless LFP recordings: A.B., J.P., M.W.. Optogenetics (combined with imaging/electrophysiology, via cranial window/cannulas): M.K., B.M., M.W., A.N.H., T.T., N.B., S.M.. Immunohistochemistry and confocal microscopy: L.K., M.B., Š.G., M.S-S., A.B., J.P.. TMEV was produced and provided by I.G. and W.B.. All murine data processing and analyses were carried out by B.M. and M.W., except: Multimodal 1-photon imaging experiments: S.M., N.B.. Tetrode recordings: A.N.H., L.E., A.G.G., M.K.. Immunohistochemistry and confocal microscopy: L.K., M.B., Š.G., M.S-S., A.B., J.P.. Processing and analysis of human recordings:

A.G,G., M.W., F.M.. H.B., R.S., and F.M. provided infrastructure, experimental, analytical, and clinical expertise.

Supplementary Materials:

Materials and Methods

Figures S1 to S11

Tables S1 to S3

Movies S1 to S7